Harlov, D. E., Anczkiewicz, R., Dunkley, D. J. (2023): Metasomatic alteration of zircon at lower crustal P-T conditions utilizing alkali- and F-bearing fluids: Trace element incorporation, depletion, and resetting the zircon geochronometer. - Geochimica et Cosmochimica Acta, 352, 222-235.

https://doi.org/10.1016/j.gca.2023.05.011

Metasomatic alteration of zircon at lower crustal P-T conditions utilizing alkali- and F-bearing fluids: trace element incorporation, depletion, and resetting the zircon geochronometer

Daniel E. Harlov[1,2,3*], Robert Anczkiewicz[4], and Daniel J. Dunkley[5,6]

[1]Deutsches GeoForschungsZentrum-GFZ, Telegrafenberg, 14473 Potsdam, Germany

[2]School of Earth Resources, China University of Geosciences, Wuhan 430074, China

[3]Department of Geology, University of Johannesburg P.O. Box 524, Auckland Park, 2006 South Africa

[4]Institute of Geological Sciences, Polish Academy of Sciences, Krakow Research Centre, Senacka 1, 31-002 Krakow, Poland

[5]Department of Polar and Marine Research, Institute of Geophysics, Polish Academy of Sciences Księcia Janusza 64, PL-01452 Warsaw, Poland

[6]National Institute of Polar Research, 3-10 Midori-cho, Tachikawa-shi, Tokyo-to, 190-8518 Japan

*dharlov@gfz-potsdam.de

ABSTRACT

Natural alteration of zircon takes place in melts or fluids either via dissolution coupled with overgrowth or via a coupled dissolution-reprecipitation process. The latter results in the zircon being partially or totally replaced by new, compositionally re-equilibrated zircon or a new mineral phase or both. In this study, fragments (50 – 300 μm) from a large, inclusion-free, clear, 520 to 530 Ma euhedral zircon with light radiation damage from a nepheline syenite pegmatite, Seiland Igneous Province, northern Norway, were experimentally reacted in 20 mg batches with 5 mg of

ThO_2 + $ThSiO_2$ + SiO_2 and a series of alkali-bearing fluids in sealed Pt capsules at 900 °C and 1000 MPa for 6 to 11 days in the piston cylinder press using a CaF_2 setup with a cylindrical graphite oven. ThO_2 + $ThSiO_2$ + SiO_2 was present at the end of the experiment. In experiments involving H_2O, H_2O + NaCl, H_2O + KCl, and 2N KOH, no reaction textures formed other than a slight dissolution of the zircon grain fragments. Experiments involving 2N NaOH, $Na_2Si_2O_5$ + H_2O, and NaF + H_2O resulted in zircon reaction textures with varying degrees of intensity, which took the form of partial replacement by compositionally modified zircon via a coupled dissolution-reprecipitation process. In the NaF + H_2O experiment some overgrowth also occurred. Altered zircon is separated by sharp compositional boundaries from unaltered zircon. Secondary ion mass spectrometry (SIMS) and laser ablation inductively coupled plasma mass spectrometry (LA-ICP-MS) analysis indicates that, relative to the unaltered zircon, the altered zircon is strongly enriched in Th, and heavily to moderately depleted in U and (Y+REE). In all the experiments, ^{206}Pb (3 to 5 ppm in unaltered zircon) is depleted in the altered zircon to below the SIMS detection limit and to at or below the LA-ICP-MS detection limit. Hafnium and Ti concentrations in the altered zircon retained the same approximate value (within error) as the original zircon. The results from these experiments demonstrate that zircon can be compositionally modified by alkali-bearing and alkali-F-bearing fluids via a coupled dissolution-reprecipitation process. Near to total loss of radiogenic Pb via such processes under high-grade conditions resets the internal zircon geochronometer. Although the end result is the same as with zircon overgrowth, i.e. the production of new generation zircon at the time of a metasomatic/metasomatic event, such replacement processes can explain incomplete isotopic ‘resetting’; inclusion production through unmixing of solid solutions in metastable zircon compositions; and ‘ghost’ textures that preserve initial growth features but with isotopic disturbance. Diagnostic replacement features produced in experiments, such as interface geometries between altered and unaltered zircon, provide markers of the mechanism and aid in zircon interpretation. A major implication from this study is that if zircon with low radiation damage can be metasomatically altered under high-grade conditions this would have important

consequences with respect to zircons presumed role as an impregnable container for mineral inclusions. Namely the mineral inclusions contained within zircon could also be altered, reset as a geochronometer, or even replaced by another mineral.

Keywords: zircon, Th, U, Pb, REE, petrochronology, coupled dissolution-reprecipitation, alkali-bearing fluids, experimental petrology

1. Introduction

In nature zircon is one of the principal accessory minerals used for the dating of geologic processes. Its chemically and mineralogically robust nature allows it to survive its igneous origins and be re-incorporated into either successive igneous protoliths, through melting of zircon-bearing source rocks, or into sedimentary protoliths, as detritus. Zircon can also survive metamorphism, metasomatism, and/or partial melting of the host rock. However, such survival is typically partial. The cores of the zircon grain tend to preserve its origins whereas the rims and replacement textures can record changes wrought during diagenesis, metasomatism, metamorphism, and re-incorporation into a magma (e.g. Harlov et al., 2022).

Zircon is a principal host for U, Th, Hf, Y, and HREEs in various sedimentary, metamorphic, and igneous rocks, and as such can contain a significant fraction of the whole rock abundance of these elements depending on the presence or lack of other minerals such as monazite, xenotime, allanite, apatite, and garnet. Despite its reputation as a refractory mineral, zircon can interact with diverse fluids and/or melts under a range of crustal P-T conditions. For example, the chemical stability of metamict zircon, radiation-damaged zircon, and synthetic (pristine) zircon with respect to various fluids has been explored experimentally as well as speculated upon in a series of studies of natural examples utilizing a variety of analytical techniques, as summarized in Geisler et al. (2007); see also Pidgeon et al. (1966), Rizvanova et al. (2000), Geisler et al. (2002, 2003), Tomaschek (2004, 2010), Lenting et al. (2010), and Lewerentz et al. (2019). Both experimentally

and in nature, compared to pristine zircon or zircon with a low degree of radiation damage, metamict zircon and zircon with a high degree of radiation damage is highly susceptible to fluid-assisted alteration down to relatively low P-T conditions (e.g., 175 °C and 250 bars) (Geisler et al., 2007).

In addition to metamict and radiation damaged zircon, reaction textures, presumed to be produced by fluids or melts, can also be seen in zircons with a low degree of radiation damage from both igneous and high-grade metamorphic rocks under cathodoluminescence (CL) imaging. Examples include zircons from a ca. 983 Ma anorthosite, Eastern Ghats Mobile Belt, India (Chatterjee et al., 2008); orthopyroxene-bearing granulite-facies granitoids (charnockites) from the Shevaroy Massif, southern India (Harlov et al., 2022); polymetamorphic migmatites, Valle d'Arbedo, Switzerland (Vonlanthen et al., 2012); granulite-facies meta-granitoids, Queensland, Australia (Hoskin and Black, 2000); and granitic gneisses in a contact aureole associated with the Rogaland anorthite-norite intrusive complex, southern Norway (Möller et al., 2002). Here CL-bright or CL-dark areas of apparent alteration overprint the original magmatic zoning (Fig. 1). The irregular and/or lobate shapes of these altered areas, which extend inward into the zircon from the grain rim, are difficult to ascribe to overgrowth of either the original zircon grain or partially dissolved zircon grain, but rather resemble the partial replacement textures in monazite that have been shown to be the result of fluid-induced coupled dissolution-reprecipitation processes as opposed to overgrowth (Harlov et al., 2011).

In this study, fragments of an inclusion-free, faintly banded zircon (CL imaging) with light radiation damage from the Seiland Igneous Province, northern Norway (Fig. 2) are used in a series of piston cylinder metasomatism experiments involving both pure H_2O and a variety of alkali-bearing solutions at 900 °C and 1000 MPa. A $ThSiO_4$ + ThO_2 + SiO_2 mix was added to all of the experiments with the goal of seeing whether or not Th could be metasomatically incorporated into the zircon crystal lattice replacing Zr utilizing reactive fluids. After quench and extraction, the reacted zircon grain fragments are then mounted, polished to cross section, and evaluated using

high-contrast backscattered electron (BSE) imaging, CL imaging, transmission electron microscopic (TEM) imaging, electron microprobe (EMP) analysis, sensitive high-resolution ion microprobe (SHRIMP) analysis, and laser ablation inductively coupled plasma mass spectrometry (LA-ICP-MS) analysis. The results from the experimentally reacted zircons are then compared with metasomatically altered zircons from nature and the reaction textures are interpreted chemically, physically, and from a petrochronological perspective.

2. Experimental and Analytical Procedures

2.1 Experimental protocol

Experiments were run at 900 °C and 1000 MPa using the two piston cylinder apparatus as described by Johannes et al. (1971) and Johannes (1973) and are summarized in Table 1. The zircon chosen for the experiments was obtained from the Natural History Museum at the University of Oslo, Oslo, Norway. It consists of a large (2 cm), transparent, inclusion-free, light brownish, euhedral crystal fragment from a nepheline syenite pegmatite located in the Seiland Magmatic Province, northern Norway (523 ± 2 to 531 ± 2 Ma; Pedersen et al., 1989). A fragment of this crystal was broken up into 50 to 300 μm size irregular grains. The transparent, inclusion-free, lightly brown-pink grain fragments were washed in ethanol in an ultrasonic bath. Size sorting was not done. High contrast BSE and CL imaging reveal that the grains are totally texture-free except for a very faint magmatic zoning (Fig. 2).

Solids in the experimental charge consisted of 20 mg of zircon, 5 mg of a $ThSiO_4$ + ThO_2 + SiO_2 mix, and 5 mg of fluid (Table 1). Reactants in the experimental charge included doubled distilled nanopore H_2O, NaCl + H_2O, KCl + H_2O, 2N NaOH, 2N KOH, $Na_2Si_2O_5$ + H_2O, and NaF + H_2O. All chemicals used were spec pure to 99.99% or better. The experimental charge was placed in a 3 mm wide, 1 cm long, tempered (1000 °C) Pt capsule, which was arc-welded shut and placed vertically, four at a time, in a CaF_2 setup with a cylindrical graphite oven (Fig. 3). The capsules were separated from each other by thin sheets of biotite. The presence of a graphite oven under the

airtight conditions of the experiment implies that the system/experiments, at least in theory, should have been buffered to graphite-CO-CO_2 once the oven was heated to 900 °C. The thermocouple tip was placed such that it reached halfway up alongside the Pt capsules (Fig. 3). The temperature differential along the capsules was approximately 40 °C with either capsule end at 860 °C compared to the sweet spot at the center of the capsules at the measured 900 °C. The pressure measured during the experiment was corrected for friction due to the CaF_2 pressure medium. Non-isobaric quench was achieved within 20 to 30 seconds by turning off the current.

After each experiment, the Pt capsule was cleaned, weighed, and punctured. The Pt capsules were then dried at 105 °C for several hours, and weighed again to determine fluid loss. Due to the very small amounts of fluid used in the experiments (5 mg), accurate trace element analysis of the fluid was not possible. The reacted charge was then carefully removed from the Pt capsule with as little mechanical disturbance as possible. The charge was then mounted and polished down to cross section in an epoxy grain mount.

2.2 Scanning electron microscope (SEM)

Experimental charges were first evaluated using high contrast BSE and CL imaging on a JEOL JSM–5900LV Scanning Electron Microscope (SEM) equipped with a Gatan MiniCL detector and JEOL SmileStation stage automation and image-capture software at the National Institute for Polar Research (NIPR), Tachikawa-shi, Tokyo-to, Japan.

2.3 Electron probe microanalysis (EPMA)

Electron probe microanalysis (EPMA) of zircon was carried out using the JEOL electron hyperprobe with field emission gun at the GeoForschungsZentrum (GFZ) Potsdam using an accelerating voltage of 15 kV and beam current of 15 nA. Individual spot analyses were made using a focused electron beam with a diameter of 1 micron. Elements analyzed for in zircon included P, Si, Ti, Zr, Hf, Th, U, Y, Gd, Tb, Dy, Ho, Er, Yb, Lu, Ca, Pb, and Na, with counting

times of 20 to 120 seconds depending on the relative amount of the element. Standards for the REE were taken from synthetic REE phosphates prepared by Jarosewich and Boatner (1991). The remaining standards were taken from both the CAMECA and Smithsonian standard sets (Jarosewich et al., 1980). The full EMP analysis data set is contained in Table S1.

2.4 Sensitive high-resolution ion microprobe (SHRIMP)

2.4.1 Zircon U-Th-Pb measurement

Mounted zircon grains were cleaned to eliminate surface contamination by common Pb, and coated with 100 Angstroms of high-purity gold. Mounts were imaged at high resolution by CL and BSE with a JEOL JSM–5900LV Scanning Electron Microscope (SEM) equipped with a Gatan MiniCL detector and JEOL SmileStation stage automation and image-capture software, at NIPR, Tachikawa-shi, Tokyo-to, Japan.

Spots were carefully chosen from SEM imaging for Th, U, and Pb analysis during multiple sessions by a SHRIMP-II at NIPR, using a primary O_2-ion beam with a typical sample surface current of 4 to 7 nA to produce 25 to 30 µm long, flat-floored oval pits. Secondary ionization was measured on a single electron multiplier on mass stations 196 (Zr_2O) through to 254 (UO), with a mass resolution of > 5000 for $^{238}U^{16}O$ and a sensitivity on ^{206}Pb of 17 to 20 cps per ppm per nA of primary current. Mass stations were measured through 5 to 6 cycles, with typical count times of 10 s per cycle for ^{204}Pb, background (at 204.04 amu) and ^{206}Pb, and 20s for ^{207}Pb. Reduction of raw data for standards and samples was performed using the SQUID v.1.12a (Ludwig, 2001), and Isoplot v.3.71 (Ludwig, 2003) add-ins for Microsoft Excel 2003. Abundance of U was calibrated against in-house reference zircon YBr157 (580 ppm U, as estimated by TIMS; provided by Allen Kennedy of the John de Laeter Centre, Curtin University of Technology, Western Australia, Australia). Corrections for common Pb on U/Pb values and ages were done with the common Pb estimated from ^{204}Pb counts and the Stacey and Kramers (1975) common Pb model for the approximate U-Pb age for each analysis. $(Pb/U)/(UO/U)^2$ values were calibrated against

measurements on reference zircon TEMORA-2 (417 Ma; Black et al., 2004). Zircon SHRIMP mean U-Th-Pb data for the reacted zircons listed in Table 1 is contained in Table 2. The full SHRIMP analytical U-Th-Pb zircon data set is contained in Table S2.

2.4.2 Zircon Y+REE analysis

Yttrium, REEs, and Hf contents were estimated for a subset of U-Th-Pb isotopic analyses by re-analyzing the same spots (Table 2). Considering the small penetration depth (< 3 micron) of the SHRIMP analytical spots, and the lack of strong chemical zoning ion in the starting material these contents are considered to be equivalent to those in zircon analyzed for U-Th-Pb. Spot sizes and mass resolutions were the same as for age analyses, with each station measured for 10 s through 6 cycles. To minimize the interference of LREE-MREE oxide peaks on MREE-HREE and Hf measurements, energy filtering was applied to reduce ^{180}Hf to 10% of the unfiltered signal. This reduces potential REEO^{+} interference to less than 1% of the unfiltered signals. Counts were normalized against ^{92}Zr from the NIST610 standard glass, and compared periodically against published values for zircon reference material 91500 (Wiedenbeck et al., 2004; Iizuka and Hirata, 2004). All estimates were within 10% of published values. Zircon SHRIMP mean REE data for the reacted zircons listed in Table 1 is contained in Table 2. The full SHRIMP analytical zircon REE data set is contained in Table S3. Chondrite-normalized REE plots of the SHRIMP REE data are contained in Figure S1.

2.5 Laser ablation inductively coupled plasma mass spectrometry (LA-ICP-MS)

Trace element abundances in zircon were measured at the Institute of Geological Sciences, Polish Academy of Sciences, Kraków Research Centre, Krakow, Poland using an ArF excimer laser-ablation system RESOlution M50 by Resonetics coupled with a quadrupole ICP-MS XSeriesII by FisherScientific. Ablation took place in a double volume Laurine technology cell in pure He (flow rate of 0.9 L/min), for which the Ar nebuliser gas (flow rate of 0.5 – 0.55 L/min) was mixed

downstream from the sample cell. After passing through a signal-smoothing manifold, the analyte was delivered to the ICP source. A small addition of nitrogen (0.005 – 0.008 L/min) was used to enhance the sensitivity of the ICP-MS. The oxide to metal ratio $^{248}ThO/^{232}Th$ was kept below 0.5 %. Analyses were performed using a rotating rectangular slit with a length of 50 µm and a width of 8 and 16 µm. An energy density of 4 to 5 J/cm^2 at a repetition rate of 5 Hz was applied. Twenty seconds of gas blank was measured prior to each 30 s ablation, which was followed by 30 s washout time. Sample runs were bracketed by measurements of the NIST 612 glass (Jochum et al., 2011). The zircon reference material 91500 (Wiedenbeck et al., 2004; Iizuka and Hirata, 2004) was frequently measured as a secondary standard along with the unknowns. The ZrO_2 content from previously acquired electron microprobe analyses of the Seiland zircon (ZrO_2 = 66.65; SiO_2 = 32.20; HfO_2 = 0.70) was used as an internal standard (Table S1). Data processing was performed using the Glitter 4.0 software from Macquarie University, Australia (Griffin et al., 2008). Zircon LA-ICP-MS mean U-Th-Pb and REE analyses for the reacted zircons listed in Table 1 is contained in Table 3. The full LA-ICP-MS analytical U-Th-Pb and REE zircon data set is contained in Table S4.

2.6 Transmission electron microscopy (TEM)

Reacted zircon grains, suitable for TEM investigation, were first selected using BSE and SEM images. Sampling was accomplished by using focused ion beam (FIB) milling (Wirth, 2004, 2009). FIB preparation was conducted under ultra-high vacuum conditions in an oil-free vacuum system using a FEI FIB200 instrument at the GeoForschungsZentrum Potsdam. TEM-ready foils of approximately 15 x 8 x 0.15 µm representing cross sections perpendicular to and across the reaction front (separating the altered and unaltered zircon) were sputtered directly from the zircon grain in the epoxy grain mount using a 30 kV Ga-ion beam. The TEM foil was protected from sputtering by the Ga-ion beam by a 1 µm thick, Pt layer deposited using a high-purity organic Pt gas ($C_9H_{16}Pt$, 99.9 %), which decomposes under the Ga-ion beam. Once cut, the TEM foils were placed on a

perforated carbon film, which was placed on a copper grid. Carbon coating to prevent charging in the TEM was not applied.

TEM on the zircon foils was carried out in a TECNAI F20 XTwin instrument operated at 200 kV and equipped with a FEG electron source. The TEM is equipped with a Gatan imaging filter (GIF Tridiem), a Fishione high-angle annular dark field detector (HAADF), and an EDAX X-ray analyzer with an ultrathin window. TEM bright field images (HREM) were acquired as energy-filtered images applying a 10 eV window to the zero-loss peak.

3. Results

All experiments were run at 900 °C and 1000 MPa over periods of 144 to 192 hours (6 – 8 days). Whereas, the zircon grain fragments were a light pinkish brown before the experiment, at quench the reacted zircon grain fragments were colorless and transparent, which suggests that any radiation damage in the zircon had been healed. This is supported by a variety of annealing experiments at comparable or lower temperatures and/or pressures (cf. Nasdala et al., 2001, 2002; Montario et al., 2008; Ginster et al., 2019; Herrmann et al., 2021; Ende et al., 2021; Härtel et al., 2022). Of the eight experimental runs reported here and listed in Table 1, in those experiments involving pure H_2O, NaCl + H_2O, KCl + H_2O, and 2N KOH, the zircon did not react with the fluid, other than showing a little dissolution along the grain fragment edge. In contrast, zircon in experiments involving $Na_2Si_2O_5$ + H_2O (Fig. 4), 2N NaOH (Fig. 5), and NaF + H_2O (2 experiments; Table 1, Fig. 6) developed reaction textures under CL imaging to varying degrees. In each of these experiments, due to the relatively large amount of the $ThSiO_4$ + ThO_2 + SiO_2 mix added (Table 1), all three phases persisted to the end of the experiment and were visible in the reacted charge.

While not obvious in high contrast BSE images, under CL imaging the altered areas in these four experimental runs appear lighter (CL-light) than the unaltered areas (CL-dark). CL-light areas are separated from CL-dark areas by sharp boundaries. In the experiments involving $Na_2Si_2O_5$ + H_2O (ZF-5; Fig. 4) and 2N NaOH (ZF-9; Fig. 5), the reaction textures are considerably less

extensive than in runs involving NaF + H_2O (ZF-16, ZF-40; Fig. 6). In the case of run ZF-9, only two zircon fragments with a reaction texture were found amongst 30 grain fragments exposed in the polished mount, which makes up about half of the total experimental product. In the case of ZF-5, about half of the grains in the grain mount had reaction textures. In contrast, in the NaF + H_2O experiment (ZF-16, ZF-40), all the zircon grains developed reaction textures ranging from slight to extensive. In runs ZF-5 and ZF-9, a lack of crystal face formation and the preservation of irregular grain fragment boundaries would suggest that the reaction textures are due to the replacement of the original zircon by altered zircon. In runs ZF-16 and ZF-40, the development of new crystal faces as a product of overgrowth is evident on some of the grains (e.g. Fig. 6a). However, reaction textures have also developed that are lobate and convex inwards, away from edges of zircon grain regardless of whether they have overgrowths or not (e.g. Figs. 6a,c,d). A second type of reaction texture occurs along cracks and possible cleavage planes inside of the zircon grains, which extends outwards from the crack into the zircon (Figs. 6e,f). There is a general lack of crystal face formation despite the fact that, due to the high ratio of fluid to zircon grain fragments by mass (Table 1), each individual grain was totally surrounded by fluid during the experiment and, hence, not in direct contact with any of the other grains unless it was overgrown by a neighboring grain (e.g. Fig. 6a).

TEM bright field images of foils sampled across the reaction front, as defined by CL imagery, in zircon grains from runs ZF-5 (Figs. 4a,b), ZF-9 (Figs. 5a,b), and ZF-16 (Figs. 6a,b), show no differences in texture on the sub-micron scale between the altered and unaltered areas in the zircon, no mineral inclusions, nor any evidence of a boundary or reaction front between the unaltered and altered zircon.

In general, both SHRIMP and LA-ICP-MS spot analyses indicate that the CL-light altered areas are moderately to heavily depleted in U and Y + HREE and enriched in Th relative to the CL-dark unaltered areas of the zircon grains, which retain the trace element abundances of the original zircon grain (Tables 2 and 3; Fig. 7; Fig. S1; Tables S2, S3, and S4). The low Th and U contents in the original Seiland zircon would imply that the amount of radiation damage to the crystallographic

lattice should be relatively minor after some 520 to 530 Ma (Table 3; Tables S2 and S4). One exception was ZF-5 ($Na_2Si_2O_5$ + H_2O). Here Gd showed no depletion within the altered areas (Fig. 7a, Fig. S1; Tables 3 and 4). In contrast, altered areas in all the experiments are heavily depleted in Pb to or below the detection limit in both the SHRIMP and LA-ICP-MS analytical data, whereas Hf and Ti show little difference in their abundances (within analytical error) between the altered and unaltered areas in the zircon (Tables 2 and 3; Tables S3 and S4).

4. Discussion

4.1 Formation of reaction textures in zircon

A series of previous studies have focused on the experimental alteration of zircon, though most of these have involved metamict or zircon with a high degree of radiation damage under temperatures and pressures lower than the ones considered in this study (Pidgeon et al., 1966; Geisler et al., 2001a,b, 2002, 2003, 2004, 2007; Rizvanova et al., 2000, 2007; Lenting et al., 2010; Lewerentz et al., 2019). In general, these experiments have involved a variety of fluids (H_2O, HCl, $Ca(OH)_2$ + H_2O, $CaCl_2$ + H_2O, and $AlCl_3$ + H_2O) over a broad range of temperatures (200 – 700 °C) and pressures (100 – 500 MPa). The zircon in these experiments generally shows a high degree of reactivity during the experiment due to the large amount of chemical potential energy stored in the disordered, amorphous areas in the zircon or in the radiation-damaged zircon crystallographic lattice (see discussion in Geisler et al., 2007). Other experiments at high P-T have focused on annealing of zircon in restricted chemical systems (Morales et al., 2022), the relationship between zircon and baddeleyite as a function of the Ca and Si activity in fluids (Lewerentz et al., 2019), or on the dissolution of zircon in a variety of silicate melts (Borisov and Aranovich, 2019; Baker et al., 2002; Schmidt et al., 2013) and in a series of fluids (Schmidt et al., 2006; Newton et al., 2010; Ayers et al., 2012; Wilke et al., 2012; Bernini et al., 2013; Ayers and Peters, 2018).

In this study, utilizing pressures and temperatures that are normally characteristic of the lower crust/lithospheric mantle, the goal was to partially alter a natural zircon with a low degree of

radiation damage metasomatically while at the same time incorporating Th in the altered areas. The reaction textures produced in the experimentally metasomatized zircon show a sharp contrast, both texturally and compositionally (trace elements), between the altered (CL-bright) and unaltered (CL-dark) zircon (Figs. 4, 5, and 6). The lobate intergrowths of altered zircon into the unaltered zircon as seen in Figures 6a, 6c, and 6d can be argued as not being a product of overgrowth, but rather a product of mineral replacement (see comments above). Similar textures, both lobate and otherwise, have been recognized in metasomatically altered monazite (cf. Harlov et al., 2011), xenotime (Harlov and Wirth, 2012), and apatite (Harlov et al., 2002, 2003, 2005) both experimentally and from nature, and have been interpreted as partial replacement textures due to a coupled dissolution-reprecipitation process (Putnis, 2002, 2009; Putnis et al., 2005; Putnis and Putnis, 2007; Putnis and Austrheim, 2010, 2013; Altree-Williams et al., 2015). This is especially obvious in Figures 4c, 6e, and 6f where alteration occurs along cracks and possible cleavage planes within the zircon grains as partial replacement textures extending into the zircon, similar to that seen in partial replacement textures involving experimental replacement of monazite by huttonite ($ThSiO_4$) (cf. Harlov et al., 2007, their figure 2h). During coupled dissolution-reprecipitation, the original zircon is dissolved in the presence of these alkali-bearing fluids while simultaneously being replaced by new zircon that compositionally is in thermodynamic equilibration with the fluid chemistry under the particular P-T conditions of the system. During this process, the new zircon uses the original zircon as a crystallographic template for purposes of nucleation and subsequent growth/replacement. In essence coupled dissolution-reprecipitation is the basis for mineral pseudomorphism, and is a commonly observed process in nature for many minerals. It is also the principal process by which fossilization of organic material, such as bone and wood, occurs.

In minerals, the process of coupled dissolution-reprecipitation has been shown to occur along a very thin (10 nm wide or less) fluid-filled reaction front between the original dissolving mineral and the newly growing mineral (Putnis, 2002, 2009; Altree-Williams et al., 2015). This reaction front is physically connected to the fluid surrounding the mineral grain via an actively

evolving, non-static, interconnected porosity prevalent throughout the newly grown mineral phase. This allows for active fluid-aided mass transfer between the fluid along the reaction front and the fluid surrounding the grain during the replacement process. Porosity formation can result from a variety of causes such as differences in the molar volume between the original and replacement phase or differences in solubility between the two phases (Putnis, 2009). Once this replacement process stops due to changing P-T-X conditions in an open fluid-mineral system or, in the case of a closed system, due to limited amounts of the reactive fluid (e.g. the experiments in this study), the reaction front will cease to advance and the altered areas of the mineral will begin to recrystallize such that the original interconnected porosity will evolve into isolated nano- and micron-size fluid inclusions often along with mineral inclusions, both those genetically derived from the host mineral and those originating from minerals outside of the host mineral (Putnis, 2002, 2009; Harlov et al., 2005, 2011; Harlov and Wirth, 2012; Harlov et al., 2016).

As can be seen in Figures 4b, 5c, and 6b, for each of the alkali-bearing fluid-zircon metasomatism experiments, neither a remnant porosity nor mineral inclusions remain in the altered areas of the zircon under CL imaging nor in TEM foils taken perpendicular to the reaction front, which includes both altered zircon and unaltered zircon. Here the reaction front, so clearly visible under CL imaging, is not visible in the TEM foils, i.e. the altered zircon appears texturally indistinguishable from the unaltered zircon (cf. Figs. 4b, 5b, and 6b). This is not what is seen in the reaction textures and accompanying TEM foils taken across reaction fronts in experimentally metasomatized fluorapatite (Harlov et al., 2005), monazite (Harlov et al., 2011), and xenotime (Harlov et al., 2012) from experiments done under the same approximate P-T conditions. It is also not seen in experimentally metasomatized metamict or radiation-damaged zircon (Geisler et al., 2007), nor in metamict or radiation-damaged zircon from nature (Geisler et al., 2002, 2003, 2007). In all of these cases the metasomatically altered areas are characterized by numerous fluid inclusions and mineral inclusions, such as $ThSiO_4$, $USiO_4$, ThO_2, UO_2, ZrO_2, xenotime, feldspar, quartz, etc..

One explanation for this striking difference in zircon textures is that the alteration textures seen in Figures 4, 5, and 6 appear to be specific to zircon with low amounts of radiation damage, characteristic of the 520 to 530 Ma Seiland zircon, the high P-T conditions of the experiments, and the reactivity of the alkali-bearing and F-bearing fluid chemistry of the system. Total elimination of the porosity during the course of the experiment, after growth of the altered area had stopped, could be due to a rapid coarsening effect, which would be consistent with attaining textural equilibration driven by reduction in the surface area as defined by the interior surface area of the pores. Hence, the original porosity, which was transient to begin with, would have totally disappeared as textural equilibration was achieved, and in this particular case achieved rather quickly during the course of the experiment. Similar phenomena have been observed in the KBr-KCl-H_2O replacement experiments of Putnis et al. (2005). Rapid disappearance of the porosity would have also discouraged mineral inclusion formation since the pores normally act as nucleation sites for inclusions in the altered/reacted areas (see discussion in Harlov et al., 2005). What overgrowth that did occur was also totally recrystallized as per the above mechanism eliminating any porosity that might have formed during crystal growth outwards. The sharp compositional boundary seen between the altered zircon and unaltered zircon under CL imaging would indicate that element diffusion across the boundary was negligible at 900 °C and 1000 MPa over the course of the experiment. This observation agrees with the U, Th, and Hf diffusion experiments of Cherniak et al. (1997a) and REE diffusion experiments of Cherniak et al. (1997b), both of which indicate very slow diffusion rates at high temperatures for these elements in zircon.

Comparison of the reaction textures resulting from the experiments (Figs. 4 – 6) with similar textures in natural zircons in Figure 1 support the proposition that high-grade, high pH, alkali-bearing/F-bearing fluids could have been responsible for them. The examples provided in Figure 1 are found in both metamorphic and igneous rocks in a fluid-rich environment with broadly granitoid and hence alkali-rich compositions or else are associated with such rocks. These observations are supported by Aranovich et al. (2017) who make a strong case for alkali-bearing fluids causing

partial to total alteration of zircon grains in gabbroids and plagiogranites from the Mid-Atlantic Ridge. In another example, zircons from a leucocratic granite of the Weondong region of South Korea show four types of partial metasomatic alteration, which the authors attribute to the action of F-rich fluids during post-magmatic alteration (Park et al., 2016; their figures 3 and 5). The textures of these metasomatised zircon grains broadly mimic some of the reaction textures obtained in the NaF-fluid experiments (Fig. 6).

4.2 Alteration of the zircon trace element chemistry

Relative to the original unaltered Seiland zircon, the altered areas in the zircon are significantly enriched in Th, significantly depleted in U, moderately to strongly depleted in Y + HREE, and nearly to totally depleted in Pb to within the detection limit of both SIMS and LA-ICP-MS. In contrast, there is little or no change in the Hf or Ti content within the measurement precision (Tables 2 and 3; Fig. 7). These abundances contrast with the fluids used in the experiments, which were saturated in Th + Si, and totally devoid of U, Pb, Y+REE, Ti, and Hf (Table 1). .

In the zircon crystallographic lattice, U^{4+}, Th^{4+}, and Hf^{4+} are conventionally considered to substitute for Zr^{4+} on the 8-fold Zr site (Finch and Hanchar, 2003; Hoskin and Schaltegger, 2003). While, Th and U have a limited solid solution with zircon as tetragonal thorite ($ThSiO_4$), and tetragonal coffinite ($USiO_4$), respectively (Ushakov et al., 1999), Hf has a complete solid solution with zircon as tetragonal hafnon ($HfSiO_4$) (Speer and Cooper, 1982). This is due to the fact that on the 8-fold Zr site Hf^{4+} (0.83 Å) can completely substitute for Zr^{4+} (0.84 Å) (effective ionic radii; Shannon, 1976; Harley and Kelly, 2007). In contrast, the relatively larger 8-fold ionic radii of U^{4+} (0.86 Å) and Th^{4+} (1.05 Å) (Shannon, 1976; Harley and Kelly, 2007), compared to 8-fold Zr^{4+} (0.84 Å), would explain their relatively limited solid solution in zircon. It would also explain as to why U^{4+} was so easily removed and Th^{4+} only incorporated in limited amounts during each of the metasomatism experiments despite the fluid being supersaturated with Th (Table 3; Tables S2 and S4).

Yttrium and the REE are generally thought to be incorporated into zircon via a xenotime-type coupled substitution or:

$$^{VIII}(Y+REE)^{3+} + {}^{IV}P^{5+} = {}^{VIII}Zr^{4+} + {}^{IV}Si^{4+} \quad (1)$$

(Finch and Hanchar, 2003; Hoskin and Schaltegger, 2003) with $(Y+REE)^{3+}$ going on the 8-fold Zr site and P^{5+} (0.17 Å) on the 4-fold Si^{4+} (0.26 Å) site (effective ionic radii; Shannon, 1976). Other possible coupled substitutions for (Y+REE) in zircon which have been described in the literature include:

$$Li^{+}_{(interstitial)} + {}^{VIII}(Y+REE)^{3+} = {}^{VIII}Zr^{4+} \quad (2)$$

(Finch et al., 2001; Wang and Trail, 2022), and:

$$H^{+}_{(interstitial)} + {}^{VIII}(Y+REE)^{3+} = {}^{VIII}Zr^{4+} \quad (3)$$

(Trail et al., 2016) where Li and H substitute on interstitial sites in the zircon structure (Finch and Hanchar, 2003). In all of these cases, 8-fold $(Y + HREE)^{3+}$ (1.019, 1.079 – 0.977 Å) are strongly preferred over the 8-fold $LREE^{3+}$ (1.160 – 1.109 Å) due to their better fit on the 8-fold Zr (0.84 Å) site (Hoskin and Schaltegger, 2003; Shannon, 1976).

From the LA-ICP-MS data in Table S4, $(Y+HREE)^{3+}$ plus the approximate value for P^{5+} when plotted vs. $Zr^{4+} + Si^{4+}$ for both unaltered and altered zircon in each of the experiments show an approximate linear relationship with a positive shallow slope. This indicates that an additional coupled substitution mechanism must have been responsible for Y+HREE incorporation in both the altered and unaltered zircon. These additional mechanisms could have included coupled substitutions (2) and/or (3), each to varying degrees, though this must be treated as speculation since neither Li nor H^{+} were measured.

The observation that Ti was not depleted in the altered areas (Table 3) is more curious considering that the alkali-bearing solutions in each of the experiments were not buffered by rutile, i.e. TiO_2, or some other Ti-rich mineral such as ilmenite or titanite; though each of the solutions was buffered to an SiO_2 activity of 1 due to the presence of free SiO_2 in the capsule at the end of the experiment. In zircon, relatively limited amounts of Ti, as $^{IV}Ti^{4+}$ (0.42 Å) are believed to substitute

for $^{IV}Si^{4+}$ (0.26 Å) (effective ionic radii; Shannon, 1976) on the tetrahedral site with the amount of Ti present increasing as a function of increasing temperature for a system nominally buffered at a constant TiO_2 activity (Watson and Harrison, 2005; Watson et al., 2006; Ferry and Watson, 2007; Harley and Kelly, 2007; Tailby et al., 2011). The fact that Ti remained in the altered areas of the zircon at 900 °C and 1000 MPa in a Ti-free system (Table 1), as opposed to selectively partitioning into the solution, would suggest that for minor amounts of Ti, the partitioning coefficients for NaF-, NaOH-, and $Na_2Si_2O_5$-bearing solutions apparently favor Ti remaining on the tetrahedral site in zircon at the P-T of the experiments. Such an observation could have implications for the Ti-in-zircon geothermometer in alkali fluid-bearing systems whether they are buffered with respect to TiO_2 or not (cf. Ferry and Watson, 2007).

Lead appears to be broadly incompatible in the zircon structure with respect to substitution on either the tetrahedral Si site or the octahedral Zr site due to its much larger size, i.e. $^{IV}Pb^{4+}$ (0.65 Å) vs. $^{IV}Si^{4+}$ (0.26 Å) and $^{VIII}Pb^{4+}$ (0.94 Å) vs. $^{VIII}Zr^{4+}$ (0.84 Å) (effective ionic radii; Shannon, 1976; Watson et al., 1997; Mezger and Krogstad, 1997; Geisler et al., 2003; Utsunomiya et al., 2004; Kogawa et al., 2012). This assumes that Pb would occur as Pb^{4+} in the zircon structure, which would seem highly unlikely assuming that the experiments were presumably buffered to graphite-CO_2 (see above). If Pb in the original, unaltered zircon existed only as Pb^{2+}, in addition to there being a question of charge balance, the misfit of Pb on both the Si and Zr sites becomes even greater, i.e. 0.98 vs. 0.26 Å and 1.29 vs. 0.84 Å, respectively. This would imply that the only Pb present in the original zircon should be from the radioactive decay of U, Th, and their short-lived daughter isotopes in the form of small accumulations in amorphous radiation-damaged domains and/or along cleavage planes, or as nano-inclusions in annealed zircon (Geisler et al., 2003; Nasdala et al., 2005; Kogawa et al., 2012; Seydoux-Guillaume et al., 2015; Valley et al., 2014, 2015; Lyon et al., 2019). A similar case has been made for Pb accumulation in monazite (Fougerouse et al., 2018). The fact that Pb is so readily removed from the altered areas of the zircon to the extent of being at or below the detection limits of both LA-ICP-MS and SIMS implies that Pb, at least in

trace amounts, is apparently highly soluble in NaF-, NaOH-, and $Na_2Si_2O_5$-bearing fluids at 900 °C and 1000 MPa most likely due to complexing with either OH^- or F^- in solution (Bottari and Ciavatta, 1965; Perera et al., 2001).

The addition of Th, loss of U, and near to total loss of Pb in the altered areas of the zircon would imply that the U-Th-Pb geochronometer has been near to totally reset compared to the unaltered areas. This obviously has major implications with regard to zircon geochronology. Namely that the zircon U-Th-Pb geochronometer can be metasomatically reset, which is an idea that has long been speculated upon in the literature (Hoskin and Schaltegger, 2003; Hoskin, 2005; Geisler et al., 2007; Soman et al., 2010; Van Lankvelt et al., 2016; Peterman et al., 2016; Aranovich et al., 2017; Chen and Zhou, 2017; Wang et al., 2018; Zi et al., 2022). Natural resetting of this geochronometer via Pb diffusion in zircon under fluid-absent conditions has been demonstrated to be a very slow, almost negligible process even if the zircon experiences relatively high temperatures (> 900 °C) for at least 1 Myr (Möller et al., 2002; see also Cherniak and Watson, 2000). In the experiments from this study, the geochronometer was reset due to alkali-bearing high pH or alkali-fluoride fluids at 900 °C and 1000 MPa over a period of days. Such fluids might explain the zircon alteration textures seen in Figure 1 since each of these examples occur in granitoid rocks rich in alkali-bearing feldspars, which have experienced metasomatism/metamorphism under high-grade conditions. In each of these cases, the CL-bright metasomatized areas tend to be younger by some millions to 10's of millions of years than the CL-dark zircon cores, which the authors generally tend to attribute to metamorphic/metasomatic processes. Similar conclusions were reached by Lewerentz et al. (2019) in experiments (600 – 900 °C; 600 – 1000 MPa) involving the partial alteration of a natural zircon in $CaCl_2$- and $Ca(OH)_2$-bearing fluids to baddeleyite. While the newly formed baddeleyite and altered areas in the zircon contained U, Th, and Y + REE derived from the zircon, Pb in both the baddeleyite and the altered areas of the zircon was below the detection limit of the SIMS.

The depletion of the Y + HREE in the altered areas of the zircon (Fig. 7) is due in part to the fact that the alkali-bearing fluids used in these experiments contained negligible amounts of REE. This apparently allowed for a fraction of the Y+HREE to be partitioned into the fluid where they presumably complexed with OH^- (ZF-5 and ZF-9) (Haas et al., 1995; Wood et al., 2002; Pourtier et al., 2010; Perry and Gysi, 2018) and/or with F^- (ZF-16 and ZF-40) (Haas et al., 1995; Tropper et al., 2011, 2013; Mair et al., 2017). Depletion or enrichment of REE in zircon is a commonly observed phenomena in granitoid rocks and generally presumed due to metasomatically induced alteration via fluids and/or melts. Examples include zircons with metasomatically altered areas depleted in REE from fluid-induced charnockite patches in granitoid rocks from Kottavattom, Trivandrum Block, southern India (Taylor et al., 2014); metasomatically altered areas depleted in REE in metamorphosed zircons from the leucocratic portion of a migmatite, Ticino, Switzerland (Vonlanthen et al., 2012); and zircons from high grade metagranitoids, Queensland, Australia where the metasomatically altered areas are depleted in REE (Hoskin and Black, 2000).

5. Summary and implications

In this study it has been demonstrated in a series of experiments that natural zircon with relatively small amounts of radiation damage can be metasomatically altered using alkali- and F-bearing solutions under the high grade P-T conditions commonly found in the lower crust. This involved the incorporation of Th and the removal of U and REE, and the near to total removal of Pb to below LA-ICP-MS and SIMS detection limits in the altered areas, which implies a basic resetting of the U-Th-Pb geochronometer. If this is also the case for zircons in nature, then this would imply that similar textures, as illustrated in Figure 1, could be metasomatically induced and thus could potentially be used to date metasomatic events.

A second major implication from these experiments is that if zircon with low radiation damage can be metasomatically altered this would have important consequences with respect to zircons presumed role as an impregnable container for mineral inclusions. Namely the mineral

inclusions contained within the zircon could also be altered, reset as a geochronometer, or even replaced by another mineral. This has important consequences especially with respect to how the mineral inclusions within the Hadean detrital zircons from Jack Hills, Australia have been utilized in an attempt to discern the geochemical and physical conditions on the very early Earth during the Hadean period (4.0 – 4.54 Ga) (Mojzsis et al., 2001; Wilde et al., 2001; Valley et al., 2002, 2014). The fact that these inclusions have apparently experienced varying degrees of alteration has been amply demonstrated by Rasmussen et al. (2011) who, in a study of monazite and xenotime inclusions in the 4.35 to 3.35 Ga Jack Hills detrital zircons, concluded that these inclusions formed as the result of a metamorphic event at either 2.68 or 0.8 Ga and at monazite-xenotime temperatures (Gratz and Heinrich, 1997) of around 420 to 475 °C. The Ti content of the quartz inclusions in these same zircons gave temperatures of 350 to 490 °C using the geothermometer of Thomas et al. (2010). They also noted that most of the mineral inclusions have the same composition and abundances as the minerals in the original metamorphic matrix in which the zircons were found. This is consistent with the idea that these inclusions, which include K-feldspar, albite, muscovite, and biotite, formed during metamorphism due perhaps to the replacement of what could have been originally apatite inclusions, which are one of the more common types of mineral inclusions in zircon and generally not observed in Jack Hills zircons. If this replacement of mineral inclusions did occur, it would probably have occurred via a coupled dissolution-reprecipitation process as outlined by the experiments in this study. These observations are backed by a CO_2 fluid inclusion study of the Jack Hills zircons by Menneken et al. (2017). Here the formation of these CO_2 inclusions appears to be related to a later metamorphic event as opposed to the primary igneous event presumed responsible for the genesis of the zircons.

Mineral inclusion formation in zircon grain interiors via a fluid-aided coupled dissolution-reprecipitation process are not limited to the Jack Hills zircons. For example, Troch et al. (2018) documented the fluid-aided formation, via coupled dissolution-reprecipitation, of U-Th-REE phases as mineral inclusions in trace element-rich zircons from the Island Park-Mount Jackson rhyolite,

Yellowstone volcanic field, Wyoming, USA. Similar conclusions have also been reached for ultra-high pressure mineral inclusions, such as coesite and jadeite, in zircon from a jadeite quartzite, Dabie orogen, central China (Gao et al., 2015). While the zircons here are presumed to have a detrital, igneous mid-crustal origin, the inclusions could only have formed during a fluid-rich event, perhaps as a result of coupled dissolution-reprecipitation, under the ultra-high pressure metamorphic conditions present during the continental subduction conditions experienced by the jadeite quartzite during the Dabie orogeny.

Similar conclusions have been reached for entirely different mineral systems. For example, Krause et al. (2013) documented metasomatically altered apatite inclusions in clinopyroxene from a nepheline-bearing clinopyroxenite located in the Uralian-Alaskan-type complexes of Kytlym and Nizhny Tagil, Ural Mountains, Russian Federation. Here the clinopyroxene experienced partial metasomatic alteration via coupled dissolution-reprecipitation by a $CaCl_2$-enriched saline fluid, which also altered the apatite inclusions in these areas from fluor-chlorapatite to chlor-fluorapatite giving them a composition similar to the apatites in the surrounding mineral matrix. In those areas of the clinopyroxene not metasomatically altered, the apatites retained their original fluor-chlorapatite composition. In another example, where apatite is the host mineral, the formation of magnetite and quartz inclusions in metasomatically altered areas of fluorapatite from the Pea Ridge iron oxide-apatite ore body is attributed to fluid-aided mass transfer of Fe and Si into the fluorapatite from magnetite and quartz in the surrounding mineral matrix, again during a process of coupled dissolution-reprecipitation (Harlov et al., 2016).

In all of these cases, the key point here is that the chemistry of a fluid encountered by zircon, or any other mineral, will dictate whether or not the mineral will experience alteration, and whether this alteration occurs by simple partial dissolution, overgrowth, or metasomatic alteration, either partial or total, via a coupled dissolution-reprecipitation process. This last process can also result in the total replacement of one mineral phase by another mineral phase as proposed for the inclusions in the zircon, clinopyroxene, or fluorapatite as discussed above. The pressure and

temperature under which such a process will or could occur is of less importance since nature has time on its side as opposed to the very finite lifetime of laboratory experiments (see discussion in Harlov et al., 2002, 2003, 2005).

The basic conclusion here is that if the typical sort of zircon commonly found in crustal rocks, with radiation damage ranging from light to metamict, encounters a chemically reactive fluid, such as the alkali-bearing and F-bearing fluids used in these experiments, it could be partially to totally altered chemically with respect to it trace elements including U, Th, Pb, and the Y+REE. This could result in the U-Th-Pb geochronometer in the altered areas being reset if all the Pb is removed thus allowing for the metasomatic event responsible to be dated. Just as importantly any inclusions in the altered areas of the zircon could also experience potential chemical alteration, depending on their reactivity to the fluid, with respect to both major and trace element composition, or be replaced by other minerals more in equilibrium with both the infiltrating fluid and the mineral assemblage surrounding the zircon.

Declaration of Competing Interest

The authors declare that they have no known competing financial interests or personal relationships that could have appeared to influence the work reported in this paper.

Acknowledgements

Richard Wirth and Anja Schreiber are thanked for their assistance with the focused ion beam sampling and the transmission electron microscopy. Dieter Rhede is thanked for helping to acquire the zircon EPMA data. Special thanks to Prof. Kazuyuki Shiraishi for making available the analytical facilities of the National Institute of Polar Research available to Daniel Dunkley and Daniel Harlov. Daniel Harlov was supported by an Invitational Fellowship for Research in Japan from the Japan Society for the Promotion of Science (or JSPS Invitational Fellowships for Research in Japan). Special thanks to the Polish Academy of Sciences (Polska Akademia Nauk, PAN) and the

Foundation for Polish Science (Fundacja na rzecz Nauki Polskiej, FNP) for supporting the LA-ICP-MS analytical facilities at the Krakow Research Centre (Robert Anczkiewicz) and making them available to Daniel Harlov. Comments by Rongquing Zhang and two anonymous reviewers helped to improve the manuscript.

Appendix A. Supplementary Material

The supplementary materials for this manuscript include four supplementary tables (Tables S1, S2, S3, and S4) and one supplementary figure (Figure S1). Table S1 contains all EPMA data acquired from these zircon metasomatism experiments. Tables S2, S3, and S4 contain all the raw LA-ICP-MS and SHRIMP data utilized to assemble Tables 2 and 3 and the REE chondrite-normalized plots in Figure 7 and Figure S1. In Figure S1, the chondrite normalized REE data from the SHRIMP analyses (Table S3) and the LA-ICP-MS analyses (Table S4) are plotted for comparison. Supplementary materials attached to this article can be found online at ……

References

Altree-Williams, A., Pring, A., Ngothai, Y., Brügger, J., 2015. Textural and compositional complexities resulting from coupled dissolution–reprecipitation reactions in geomaterials. Earth Sci. Rev. 150, 628–651.

Aranovich, L.Y., Bortnikov, N.S., Zinger, T.F., Borisovskiy, S.E., Matrenichev, V.A., Pertsev, A.N., Sharkov, E.V., Skolotnev, S.G., 2017. Morphology and impurity elements of zircon in the oceanic lithosphere at the mid-Atlantic ridge axial zone (6°–13° N): evidence of specifics of magmatic crystallization and postmagmatic transformations. Petrology 25, 335–361.

Ayers, J.C., Zhang, L., Luo, Y., Peters, T.J., 2012. Zircon solubility in alkaline aqueous fluids at upper crustal conditions. Geochim. Cosmochim. Acta 96, 18–28.

Ayers, J.C., Peters, T.J., 2018. Zircon/fluid trace element partition coefficients measured by recrystallization of Mud Tank zircon at 1.5 GPa and 800–1000 °C. Geochim. Cosmochim. Acta 223, 60–74.

Baker, D.R., Conte, A.M., Freda, C., Ottolini, L., 2002. The effect of halogens on Zr diffusion and zircon dissolution in hydrous metaluminous granitic melts. Contrib. Mineral. Petrol. 142, 666–678.

Bernini, D., Audètat, A., Dolejs, D., Keppler, H., 2013. Zircon solubility in aqueous fluids at high temperatures and pressures. Geochim. Cosmochim. Acta 119, 178–187.

Black, L.P., Kamo, S.L., Allen, C.M., Davis, D.W., Aleinikoff, J.N., Valley, J.W., Mundilf, R., Campbell, I.H., Korscha, I.J., Williams, I.S., Foudoulis, C., 2004. Improved $^{206}Pb/^{238}U$ microprobe geochronology by the monitoring of a trace-element-related matrix effect; SHRIMP, ID–TIMS, ELA–ICP–MS and oxygen isotope documentation for a series of zircon standards. Chem. Geol. 205, 115–140.

Borisov, A., Aranovich, L., 2019. Zircon solubility in silicate melts: New experiments and probability of zircon crystallization in deeply evolved basic melts. Chem. Geol. 510, 103–112.

Bottari, E., Ciavatta, L., 1965. On the complex formation between lead(II) and fluoride ions. J. Inorg. Nucl. Chem. 27, 133–141.

Chatterjee, N., Crowley, J.L., Mukherjee, A., Das, S., 2008. Geochronology of the 983-Ma Chilka lake anorthosite, Eastern Ghats Belt, India: implications for Pre-Gondwana tectonics. J. Geol. 116, 105–118.

Chen, W.T., Zhou, M.-F., 2017. Hydrothermal alteration of magmatic zircon related to NaCl-rich

brines: diffusion-reaction and dissolution-reprecipitation processes. Am. J. Sci. 317, 177–215.

Cherniak, D.J., Hanchar, J.M., Watson, E.B., 1997a. Diffusion of tetravalent cations in zircon. Contrib. Mineral. Petrol. 127, 383–390.

Cherniak, D.J., Hanchar, J.M., Watson, E.B., 1997b. Rare earth diffusion in zircon. Chem. Geol. 134, 289–301.

Cherniak, D.J., Watson, E.B., 2000. Pb diffusion in zircon. Chem. Geol. 172, 5–24.

Ende, M., Chanmuang N.C., Reiners, P.W., Zamyatin, D.A., Gain, S.E.M., Wirth, R., Nasdala, L., 2021. Dry annealing of radiation-damaged zircon: single-crystal X-ray and Raman spectroscopy study. Lithos 406–407, 106523.

Ferry, J.M., Watson, E.B., 2007. New thermodynamic models and revised calibrations for the Ti-in-zircon and Zr-in rutile thermometers. Contrib. Mineral. Petrol. 154, 429–437.

Finch, R.J., Hanchar, J.M., Hoskin, P.W.O., Burns, P.C., 2001. Rare-earth elements in synthetic zircon: Part 2. a single-crystal X-ray study of xenotime substitution. Am. Mineral. 86, 681–689.

Finch, R.J., Hanchar, J.M., 2003. Structure and chemistry of zircon and zircon-group minerals. Rev. Mineral. Geochem. 53, 1–25.

Fougerouse, D., Reddy, S.M., Saxey, D.W., Erickson, T.M., Kirkland, C.L., Rickard, W.D.A., Seydoux-Guillaume, A.-M., Clark, C., Buick, I.S., 2018. Nanoscale distribution of Pb in monazite revealed by atom probe microscopy. Chem. Geol. 479, 251–258.

Gao, X.-Y., Zheng, Y.-F., Chen, Y.-X., Tang H.-L., Li, W.-C., 2015. Zircon geochemistry records the action of metamorphic fluid on the formation of ultra-high-pressure jadeite quartzite in the Dabie orogen. Chem. Geol. 419, 158–175.

Gauthiez-Putallaz, L., Rubatto, D., Hermann, J., 2016. Dating prograde fluid pulses during subduction by in situ U-Pb and oxygen isotope analysis. Contrib. Mineral. Petrol. 171, 15.

Geisler, T., Ulonska, M., Schleicher, H., Pidgeon, R.T., van Bronswijk, W., 2001a. Leaching and differential recrystallization of metamict zircon under experimental hydrothermal conditions. Contrib. Mineral. Petrol. 141, 53–65.

Geisler, T., Pidgeon, R.T., van Bronswijk, W., Pleysier, R., 2001b. Kinetics of thermal recovery and recrystallization of partially metamict zircon: a Raman spectroscopic study. Eur. J. Mineral. 13, 1163–1176.

Geisler, T., Pidgeon, R.T., van Bronswijk, W., Kurtz, R., 2002. Transport of uranium, thorium, and lead in metamict zircon under low-temperature hydrothermal conditions. Chem. Geol. 191, 141–154.

Geisler, T., Pidgeon, R.T., Kurtz, R., van Bronswijk, W., Schleicher, H., 2003. Experimental hydrothermal alteration of partially metamict zircon. Am. Mineral. 88, 1496–1513.

Geisler, T., Seydoux-Guillaume, A.-M., Wiedenbeck, M., Wirth, R., Berndt, J., Zhang, M., Mihailova, B., Putnis, A., Salje, E.K.H., Schlüter, J., 2004. Periodic precipitation pattern formation in hydrothermally treated metamict zircon. Am. Mineral. 89, 1341–1347.

Geisler, T., Schaltegger, U., Tomaschek, F., 2007. Re-equilibration of zircon in aqueous fluids and melts. Elements 3, 43-50.

Ginster, U., Reiners, P.W., Nasdala, L., Chanmuang N., C., 2019. Annealing kinetics of radiation damage in zircon. Geochim. Cosmochim. Acta 249, 225–246.

Gratz, R., Heinrich, W., 1997. Monazite-xenotime thermobarometry: Experimental calibration of the miscibility gap in the binary system $CePO_4$-YPO_4. Am. Mineral. 82, 772–780.

Griffin, W., Powell, W., Pearson, N., O'Reilly, S., 2008. GLITTER: Data reduction software for laser ablation ICP-MS: Mineralogical Association of Canada Short Course, v. 40.

Haas, J.R., Shock, E.L., Sassani, D.C., 1995. Rare earth elements in hydrothermal systems: estimates of standard partial molal thermodynamic properties of aqueous complexes of the rare earth elements at high pressures and temperatures. Geochim. Cosmochim. Acta 59, 4329–4350.

Harley, S.L., Kelly, N.M., 2007. Zircon tiny but timely. Elements 3, 13–18.

Harlov, D.E., Förster, H.-J., Nijland, T.G., 2002. Fluid-induced nucleation of (Y + REE)-phosphate minerals within apatite: nature and experiment. Part I. chlorapatite. Am. Mineral. 87, 245–261.

Harlov, D.E., Förster, H.-J., 2003. Fluid-induced nucleation of REE phosphate minerals within apatite: nature and experiment. Part II. fluorapatite. Am. Mineral. 88, 1209–1229.

Harlov, D.E., Wirth, R., Förster, H.-J., 2005. An experimental study of dissolution-reprecipitation in fluorapatite: fluid infiltration and the formation of monazite. Contrib. Mineral. Petrol. 150, 268–286.

Harlov, D.E., Wirth, R., Hetherington, C.J., 2007. The relative stability of monazite and huttonite at 300–900 °C and 200–1000 MPa: metasomatism and the propagation of metastable mineral phases. Am. Mineral. 92, 1652–1664.

Harlov, D.E., Wirth, R., Hetherington, C.J., 2011. Fluid-mediated partial alteration in monazite: the role of coupled dissolution–reprecipitation in element redistribution and mass transfer. Contrib. Mineral. Petrol. 162, 329–348.

Harlov, D.E., Wirth, R., 2012. Experimental incorporation of Th into xenotime at middle to lower crustal P-T utilizing alkali-bearing fluids. Am. Mineral. 97, 641–652.

Harlov, D.E., Meighan, C.J., Kerr, I.D., Samson, I.M., 2016. Mineralogy, chemistry, and fluid-aided evolution of the Pea Ridge Fe oxide-(Y + REE) deposit, southeast Missouri, USA. Econ. Geol. 111, 1963–1984.

Harlov, D.E., Dunkley, D.J., Hansen, E.C., Ishwar-Kumar, C., Samuel, V., Hokada, T., 2022. Zircon as a recorder of trace element changes during high grade metamorphism of Neoarchean lower crust, Shevaroy Block, Eastern Dharwar Craton, India. J. Petrol. 63, egac036.

Härtel, B., Jonckheere, R., Ratschbacher, L., 2022. Multi-band Raman analysis of radiation damage in zircon for thermochronology: partial annealing and mixed signals. Geochem. Geophys. Geosys. 23, e2021GC010182.

Herrmann, M., Söderlund, U., Scherstén, A., Næraa, T., Holm-Alwmark, S., Alwmark, C., 2021. The effect of low‐temperature annealing on discordance of U–Pb zircon ages. Sci. Rept. 11, 7079.

Hoskin, P.W.O., 2005. Trace-element composition of hydrothermal zircon and the alteration of Hadean zircon from the Jack Hills, Australia. Geochim. Cosmochim. Acta 69, 637–648.

Hoskin, P.W.O., Black, L.P., 2000. Metamorphic zircon formation by solid-state recrystallization of protolith igneous zircon. J. Metamorph. Geol. 18, 423–439.

Hoskin, P.W.O., Schaltegger, U., 2003. The composition of zircon and igneous and metamorphic petrogenesis. Rev. Mineral. Geochem. 53, 27–62.

Iizuka, T., Hirata, T., 2004. Simultaneous determinations of U-Pb age and REE abundances for zircons using ArF excimer laser ablation-ICPMS. Geochem. J. 38, 229–241.

Jarosewich, E., Nelen, J.A., Norberg, J.A., 1980. Reference samples for electron microprobe analysis. Geostand. Newslett. 4, 43–47.

Jarosewich, E., Boatner, L.A., 1991. Rare-earth element reference samples for electron microprobe analysis. Geostand. Newslett. 15, 397–399.

Jochum, K.P., Weis, U., Stoll, B., Kuzmin, D., Yang, Q., Raczek, I., Jacob, D.E., Stracke, A., Birbaum, K., Frick, D.A., Günther, D., Enzweiler, J., 2011. Determination of reference values for NIST SRM 610-617 glasses following ISO guidelines. Geostand. Geoanal. Res. 35, 397–429.

Johannes, W., Bell, P.M., Mao, H.K., Boettcher, A.L., Chipman, D.W., Hays, J.F., et al., 1971. An interlaboratory comparison of piston-cylinder pressure calibration using the albite-breakdown reaction. Contrib. Mineral. Petrol. 32, 24–38.

Johannes, W., 1973. A simplified piston-cylinder apparatus of high precision. N. Jahrb. Mineral. Monat. 7, 331–351.

Kogawa, M., Watson, E.B., Ewing, R.C., Utsunomiya, S., 2012. Lead in zircon at the atomic scale. Am. Mineral. 97, 1094–1102.

Krause, J., Harlov, D.E., Pushkarev, E.V., Brügmann, G.E., 2013. Apatite and clinopyroxene as tracers for metasomatic processes in nepheline clinopyroxenites of Uralian-Alaskan-type complexes in the Ural Mountains, Russian Federation. Geochim. Cosmochim. Acta 121, 503–521.

Lenting, C., Geisler, T., Gerdes, A., Kooijman, E., Scherer, E.E., Zeh, A., 2010. The behaviour of the Hf isotope system in radiation-damaged zircon during experimental hydrothermal alteration. Am. Mineral. 95, 1343–1348.

Lewerentz, A., Harlov, D.E., Schersten, A., Whitehouse, M.J., 2019. Baddeleyite formation in zircon by Ca‐bearing fluids in silica‐saturated systems in nature and experiment: resetting of the U-Pb geochronometer. Contrib. Mineral. Petrol. 174, 64.

Ludwig, K.R., 2001. SQUID: A User's Manual: Berkeley Geochronology Center, Special Publication 2, 22 pp.

Ludwig, K.R., 2003. User's manual for Isoplot 3.00: A geochronological toolkit for Microsoft Excel: Berkeley Geochronology Center, Special Publication 4, 71 pp.

Lyon, I.C., Kusiak, M.A., Wirth, R., Whitehouse, M.J., Dunkley, D.J., Wilde, S.A., Schaumlöffel, D., Malherbe, J., Moore, K.L., 2019. Pb nanospheres in ancient zircon yield model ages for zircon formation and Pb mobilization. Sci. Rept. 9, 13702.

Mair, P., Tropper, P., Harlov, D.E., Manning, C.E., 2017. The solubility of $CePO_4$ monazite and YPO_4 xenotime in KCl-H_2O fluids at 800 °C and 1.0 GPa: implications for REE transport in high-grade crustal fluids. Am. Mineral. 102, 2457–2466.

McDonough, W.F., Sun S., 1995. The composition of the Earth. Chem. Geol. 120, 223–253.

Menneken, M., Geisler, T., Nemchin, A.A., Whitehouse, M.J., Wilde, S.A., Gasharova, B., Pidgeon, R.T., 2017. CO_2 fluid inclusions in Jack Hills zircons. Contrib. Mineral. Petrol. 172, 66.

Mezger, K., Krogstad, E.J., 1997. Interpretation of discordant U-Pb zircon ages: an evaluation. J. Metamorph. Geol. 15, 127–140.

Mojzsis, S.J., Harrison, T.M., Pidgeon, R.T., 2001. Oxygen-isotope evidence from ancient zircons for liquid water at the Earth's surface 4,300 Myr ago. Nature 409, 178–181.

Möller, A., O'Brien, P.J., Kennedy, A., Kröner, A., 2002. Polyphase zircon in ultrahigh-temperature granulites (Rogaland, SW Norway): constraints for Pb diffusion in zircon. J. Metamorph. Geol. 20, 727–740.

Montario, M.J., Garver, J.I., Marsellos, A., 2008. Annealing of radiation damage in a Grenville

zircon, from the eastern Adirondacks, NY State. In Garver, J.I., and Montario, M.J. (eds.), Proceedings from the 11th International Conference on thermochronometry, Anchorage Alaska, Sept. 2008.

Morales, I., Molina, J.F., Cambeses, A., Montero, P., Bea F., 2022. Experimental annealing of zircon: influence of inclusions on stability, intracrystalline melt migration, common lead leaching, and permeability to fluids. ACS Earth Space Chem. 6, 288–307.

Nasdala, L., Wenzel, M., Vavra, G., Irmer, G., Wenzel, T., Kober, B., 2001. Metamictisation of natural zircon: accumulation versus thermal annealing of radioactivity-induced damage. Contrib. Mineral. Petrol. 141, 125–144.

Nasdala, L., Lengauer, C.L., Hanchar, J.M., Kronz, A., Wirth, R., Blanc, P., Kennedy, A.K., Seydoux-Guillaume, 2002. Annealing radiation damage and the recovery of cathodoluminescence. Chem. Geol. 191, 121–140.

Nasdala, L., Hanchar, J.M., Kronz, A., Whitehouse, M.J., 2005. Long term stability of alpha particle damage in natural zircon. Chem. Geol. 220, 83–103.

Newton, R.C., Manning, C.E., Hanchar, J.M., Colasanti, C.V., 2010. Free energy of formation of zircon based on solubility measurements at high temperature and pressure. Am. Mineral. 95, 52–58.

Park, C., Song, Y., Chung, D., Kang, I.-M., Khulganakhuu, C., Yi, K., 2016. Recrystallization and hydrothermal growth of high U–Th zircon in the Weondong deposit, Korea: record of post-magmatic alteration. Lithos 260, 268–285.

Pedersen, R.B., Dunning, G.R., Robins, B., 1989. U-Pb ages of nepheline syenite pegmatites from the Seiland Magmatic Province, N. Norway. In Gayer, R.A., ed. The Caledonide Geology of Scandinavia. London, Graham and Trotman, pp. 3–9.

Perera, W.N., Hefter, G., Sipos, P.M., 2001. An investigation of the lead(II)-hydroxide system. Inorg. Chem. 40, 3974–3978.

Perry, E.P., Gysi, A.P., 2018. Rare earth elements in mineral deposits: speciation in hydrothermal fluids and partitioning in calcite. Geofluids 2018, 5382480.

Peterman, E.M., Snoeyenbos, D.R., Jercinovic, M.J., Kylander-Clark, A., 2016. Dissolution-reprecipitation metasomatism and growth of zircon within phosphatic garnet in metapelites from western Massachusetts. Am. Mineral. 101, 1792–1806.

Pidgeon, R.T., O'Neil, J.R., Silver, L.T., 1966. Uranium and lead isotopic stability in a metamict zircon under experimental hydrothermal conditions. Science 154, 1538–1540.

Pourtier, E., Devidal, J.-L., Gibert, F., 2010. Solubility measurements of synthetic neodymium

monazite as a function of temperature at 2 kbars, and aqueous neodymium speciation in equilibrium with monazite. Geochim. Cosmochim. Acta 74, 1872–1891.

Putnis, A., 2002. Mineral replacement reactions: from macroscopic observations to microscopic mechanisms. Mineral. Mag. 66, 689–708.

Putnis, A., 2009. Mineral replacement reactions. Rev. Mineral. Geochem. 70, 87–124.

Putnis, A., Putnis, C., 2007. The mechanism of re-equilibration of solids in the presence of a fluid phase. J. Solid State Chem. 180, 1783–1786.

Putnis, A., Austrheim, H., 2010. Fluid-induced processes: metasomatism and metamorphism. Geofluids 10, 254–269.

Putnis, A., Austrheim, H., 2013. Mechanisms of metasomatism and metamorphism on the local mineral scale: the role of dissolution-reprecipitation during mineral re-equilibration. In D.E. Harlov and H. Austrheim, Metasomatism and the Chemical Transformation of Rock, Lecture Notes in Earth System Sciences, Springer-Verlag Berlin Heidelberg, pp. 141–170.

Putnis, C.V., Tsukamoto, K., Nishimura, Y., 2005. Direct observations of pseudomorphism: compositional and textural evolution at a fluid solid interface. Am. Mineral. 90, 1909–1912.

Rasmussen, B., Fletcher, I.R., Muhling, J.R., Gregory, C.J., Wilde, S.A., 2011. Metamorphic replacement of mineral inclusions in detrital zircon from Jack Hills, Australia: implications for the Hadean Earth. Geology 39, 1143–1146.

Rizvanova, N.G., Levchenkov, A., Belous, A.E., Bezmen, N.I., Maslenikov, A.V., Komarov, A.N., Makeev, A.F., Levskiy, L.K., 2000. Zircon reaction and stability of the U-Pb isotope system during interaction with carbonate fluid: experimental hydrothermal study. Contrib. Mineral. Petrol. 139, 101–114.

Rizvanova, N.G., Gaidamako, I.M., Levchenkov, O.A., Bezmen, N.I., Makeev, A.F., Levsky, L.K., 2007. Interaction of metamict zircon with fluids of various composition. Geochem. Internat. 45, 465–477.

Schmidt, C., Rickers, K., Wirth, R., Nasdala, L., Hanchar, J.M., 2006. Low-temperature Zr mobility: an in situ synchrotron-radiation XRF study of the effect of radiation damage in zircon on the element release in H_2O + HCl ± SiO_2 fluids. Am. Mineral. 91, 1211–1215.

Schmidt, C., Steele-MacInnis, M., Watenphul, A., Wilke, M., 2013. Calibration of zircon as a Raman spectroscopic pressure sensor to high temperatures and application to water-silicate melt systems. Am. Mineral. 98, 643–650.

Seydoux-Guillaume, A.-M., Bingen, B., Paquette, J.-L., Bosse, V., 2015. Nanoscale evidence for uranium mobility in zircon and the discordance of U–Pb chronometers. Earth Planet. Sci. Lett. 409, 43–48.

Shannon, R.D., 1976. Revised effective ionic radii and systematic studies of interatomic distances in halides and chalcedonides. Acta Crystal. A32, 751–767.

Soman, A., Geisler, T., Tomaschek, F., Grange, M., Berndt, J., 2010. Alteration of crystalline zircon solid solutions: a case study on zircon from an alkaline pegmatite from Zomba–Malosa, Malawi. Contrib. Mineral. Petrol. 160, 909–930.

Speer, J.A., Cooper, B.J., 1982. Crystal structure of synthetic hafnon, $HfSiO_4$, comparison with zircon and the actinide orthosilicates. Am. Mineral. 67, 804–808.

Stacey, J.C., Kramers, J., 1975. Approximation of terrestrial lead isotope evolution by a two-stage model. Earth Planet. Sci. Lett. 26, 207–221.

Tailby, N.D., Walker, A.M., Berry, A.J., Hermann, J., Evans, K.A., Mavrogenes, J.A., O'Neill, H.St.C., Rodina, I.S., Soldatov, A.V., Rubatto, D., Sutton, S.R., 2011. Ti site occupancy in zircon. Geochim. Cosmochim. Acta 75, 905–921.

Taylor, R.J.M., Clark, C., Fitzsimons, I.C.W., Santosh, M., Hand, M., Evans, N., McDonald, B., 2014. Post-peak, fluid-mediated modification of granulite facies zircon and monazite in the Trivandrum Block, southern India. Contrib. Mineral. Petrol. 168, 1044.

Thomas, J.B., Watson, E.B., Spear, F.S., Shemella, P.T., Nayak, S.K., Lanzirotti, A., 2010. TitaniQ under pressure: the effect of pressure and temperature on the solubility of Ti in quartz. Contrib. Mineral. Petrol. 160, 743–759.

Tomaschek, F., 2004. Zircon re-equilibration by dissolution-reprecipitation: reaction textures from flux-grown solid solutions. Berichte der Deutschen Mineralogischen Geschellschaft Beihefte zum Eur. J. Mineral. 16, 147.

Tomaschek, F., 2010. Praktische Aspekte der Mischkristallphase Zirkon: Reequilibrierungsprozess, Zirkon-Xenotim Mischungslücke, geochronologische Anwendungen in einem polymetamorphen Kristallinkomplex (Syros, Kykladen, Griechenland). Ph.D. thesis Mathematisch Naturwissenschaftlichen Fakultät der Westfälischen Wilhelms-Universität Münster, Münster, Germany, 431 pp.

Trail, D., Cherniak, D.J., Watson, E.B., Harrison, T.M., Weiss, B.P., Szumila, I., 2016. Li zoning in zircon as a potential geospeedometer and peak temperature indicator. Contrib. Mineral. Petrol. 171, 25.

Troch, J., Ellis, B.S., Schmitt, A.K., Bouvier, A.-S., Bachmann, O., 2018. The dark side of zircon: textural, age, oxygen isotopic and trace element evidence of fluid saturation in the subvolcanic reservoir of the Island Park-Mount Jackson Rhyolite, Yellowstone (USA). Contrib. Mineral. Petrol. 173, 54.

Tropper, P., Manning, C.E., Harlov, D.E., 2011. Solubility of $CePO_4$ monazite and YPO_4 xenotime

in H_2O and H_2O-NaCl at 800 °C and 1 GPa: implications for REE and Y transport during high-grade metamorphism. Chem. Geol. 282, 58–66.

Tropper, P., Manning, C.E., Harlov, D.E., 2013. Experimental determination of $CePO_4$ and YPO_4 solubilities in H_2O-NaF at 800 °C and 1 GPa: implications for rare earth element transport in high-grade metamorphic fluids. Geofluids 13, 372–380.

Ushakov, S.V., Gong, W., Yagovkina, M.M., Helean, K.B., Lutze, W., Ewing, R.C., 1999. Solid solutions of Ce, U, and Th in zircon. Ceram. Trans. 93, 357–363.

Utsunomiya, S., Palenik, C.S., Valley, J.W., Cavosie, A.J., Wilde, S.A., Ewing, R.C., 2004. Nanoscale occurrence of Pb in an Archean zircon. Geochim. Cosmochim. Acta 68, 4679–4686.

Valley, J.W., Peck, W.H., King, E.M., Wilde, S.A.W., 2002. A cool early Earth. Geology 30, 351–354.

Valley, J.W., Cavosie, A.J., Ushikubo, T., Reinhard, D.A., Lawrence, D.F., Larson, D.J., Clifton, P.H., Kelly, T.F., Wilde, S.A., Moser, D.E., Spicuzza, M.J., 2014. Hadean age for a post-magma-ocean zircon confirmed by atom-probe tomography. Nature Geosci. 7, 219–223.

Valley, J.W., Reinhard, D.A., Cavosie, A.J., Ushikubo, T., Lawrence, D.F., Larson, D.J., Kelly, T.F., Snoeyenbos, D.R., Strickland, A., 2015. Nano- and micro-geochronology in Hadean and Archean zircons by atom-probe tomography and SIMS: new tools for old minerals. Am. Mineral. 100, 1355–1377.

Van Lankvelt, A., Schneider, D.A., Biczok, J., McFarlane, C.R.M., Hattori, K., 2016. Decoding zircon geochronology of igneous and alteration events based on chemical and microstructural features: a study from the Western Superior Province, Can. J. Petrol. 57, 1309–1334.

Vonlanthen, P., Fitz Gerald, J.D., Rubatto, D., Hermann, J., 2012. Recrystallization rims in zircon (Valle d'Arbedo, Switzerland): an integrated cathodoluminescence, LA-ICP-MS, SHRIMP, and TEM study. Am. Mineral. 97, 369–377.

Wang, R., Jeon, H., Evans, N.J., 2018. Archaean hydrothermal fluid modified zircons at Sunrise Dam and Kanowna Belle gold deposits, Western Australia: implications for post-magmatic fluid activity and ore genesis. Am. Mineral. 103, 1891–1905.

Wang, Y., Trail, D., 2022. Experimental partitioning of Li between zircon and different silicate melts: implications for Li contents in the Hadean and modern crust. Contrib. Mineral. Petrol. 177, 15.

Watson, B., Cherniak, D.J., Hanchar, J.M., Harrison, T.M., Wark, D.A., 1997. The incorporation of Pb into zircon. Chem. Geol. 141, 19–31.

Watson, E.B., Harrison, T.M., 2005. Zircon thermometer reveals minimum melting conditions on earliest Earth. Science 308, 841–844.

Watson, E.B., Wark, D.A., Thomas, J.B., 2006. Crystallization thermometers for zircon and rutile. Contrib. Mineral. Petrol. 151, 413–433.

Wiedenbeck, M., Hanchar, J.M., Peck, W.H., Sylvester, P., Valley. J., Whitehouse, M., Kronz, A., Morishita, Y., Nasdala, L., Fiebig, J., Franchi, I., Girard, J.-P., Greenwood, R.C., Hinton, R., Kita, N., Mason, P.R.D., Norman, M., Ogasawara, M., Piccoli, P.M., Rhede, D., Satoh, H., Schulz-Dobrick, B., Skår, O., Spicuzza, M.J., Terada, K., Tindle, A., Togashi, S., Vennemann, T., Xie, Q., Zheng, Y.-F., 2004. Further characterisation of the 91500 zircon crystal. Geostand. Geoanal. Res. 28, 9–39.

Wilde, S.A., Valley, J.W., Peck, W.H., Graham, C.M., 2001. Evidence from detrital zircons for the existence of continental crust and oceans on the Earth 4.4 Gyr ago. Nature 409, 175–178.

Wilke, M., Schmidt, C., Dubrail, J., Appel, K., Borchert, M., Kvashina, K., Manning, C.E., 2012. Zircon solubility and zirconium complexation in H_2O + Na_2O + SiO_2 +/- Al_2O_3 fluids at high pressure and temperature. Earth Planet. Sci. Lett. 349-350, 15–25.

Wirth, R., 2004. Focused ion beam (FIB): A novel technology for advanced application of micro- and nano-analysis in geosciences and applied mineralogy. Eur. J. Mineral. 15, 863–875.

Wirth, R., 2009. Focused Ion Beam (FIB) combined with SEM and TEM: advanced analytical tools for studies of chemical composition, microstructure and crystal structure in geomaterials on a nanometre scale. Chem. Geol. 261, 217–229.

Wood, S.A., Palmer, D.A., Wesolowski, D.J., B´en´ezeth, P., 2002. The aqueous geochemistry of the rare earth elements and yttrium. Part XI. the solubility of $Nd(OH)_3$ and hydrolysis of Nd^{3+} from 30 to 290 °C at saturated water vapor pressure with in-situ pHm measurement. In Water-Rock Interactions, Ore Deposits, and Environmental Geochemistry: A Tribute to David A. Crerar, R. Hellmann and S. A. Wood, Eds., vol. 7, 229–256.

Zi, J.W., Rasmussen, B., Muhling, J.R., Fletcher, I.R., 2022. In situ U-Pb and geochemical evidence for ancient Pb-loss during hydrothermal alteration producing apparent young concordant zircon dates in older tuffs. Geochim. Cosmochim. Acta 320, 324–338.

Figures

Figure 1: CL images of zircon from (**a,b**) the Shevaroy Massif (granulite-facies charnockite), Tamil Nadu, southern India (Harlov et al., 2022); (**c**) an anorthsite, Eastern Ghats Belt, India (Chatterjee et al., 2008; their Figure 2B); (**d**) polymetamorphic migmatites, Valle d'Arbedo, Ticino, Switzerland (Vonlanthen et al., 2012); (**e**) high-grade granulite-facies metagranitoids, Queensland, Australia (Hoskin and Black, 2000); and (**f**) a granitic gneiss in the contact aureole of the Rogaland anorthosite-norite intrusive complex, southwest Norway (Möller et al., 2002). Terms sz, oz, and og in Figure 1c stand for sector zoned, oscillatory zoned, and over growth, respectively. In Figure 1d, the circles 5a, 5b, 5c, and 5d indicate areas where TEM foils were cut. In Figure 1e, P stands for protolith zircon; C_1 and C_2 stands for inherited core; OZP stands for oscillatory zircon; and the scale bars are all 50 μm. Under CL imaging for all images, the light areas in the zircon are depleted in Th and U relative to dark areas in the zircon.

Figure 2: (**a**) BSE and (**b**) CL images of a grain fragment of the starting zircon from a nepheline syenite pegmatite, Seiland igneous province, northern Norway.

Figure 3: Sketch of the CaF_2 assembly used in the experiments with the piston cylinder apparatus showing the location of the four Pt capsules separated by biotite sheets.

Figure 4: (**a,c,d**) CL images of a zircon grain fragment reacted in a $Na_2Si_2O_5$ + H_2O solution + ThO_2 + $ThSiO_4$ + SiO_2 at 900 °C and 1000 MPa. Altered areas (light areas in CL) are enriched in Th and depleted in U, Pb, and (Y+REE) (see Tables 2 and 3). Figure 4b is a TEM foil taken from the elongated area located across the reaction front shown in Figure 4a. Note the lack of any reaction texture in the TEM foil nor the indication of a reaction front (the sharp boundary between

light and dark areas in Figure 4b). Dark ovals in the background are from the carbon foil upon which the TEM foil rests.

Figure 5: BSE (**a**) and CL (**b**) images of a zircon grain fragment reacted in a 2N NaOH solution + ThO_2 + $ThSiO_4$ + SiO_2 at 900 °C and 1000 MPa. Altered areas (light areas in CL) are enriched in Th and depleted in U, Pb, and (Y+REE) (see Tables 2 and 3). Figure 5b is a TEM foil taken from the elongated area across the reaction front shown in Figure 5a. Note the lack of any reaction texture in the TEM foil nor the indication of a reaction front (the sharp boundary between light and dark areas in Figure 5b). Dark ovals in the background are from the carbon foil upon which the TEM foil rests.

Figure 6: (**a,c,d,e,f**) CL images of zircon reacted in a NaF + H_2O solution + ThO_2 + $ThSiO_4$ + SiO_2 at 900 °C and 1000 MPa. Altered areas (light areas in CL) are enriched in Th and depleted in U, Pb, and (Y+REE) (see Tables 2 and 3). Figure 6b is a TEM foil taken from the elongated area across the reaction front shown in Figure 6a. Note the lack of any reaction texture in the TEM foil nor the indication of a reaction front (the sharp boundary between light and dark areas in Figure 6b). Dark ovals in the background are from the carbon foil upon which the TEM foil rests. Note also the overgrowth of zircon near the top of Figure 6a (sharp crystallographic faces) and compare this to the lack of crystallographic faces along the bottom of the grain where intergrowth occurs into the zircon body via fluid-aided coupled dissolution-reprecipitation. In Figures 6e and 6f alteration is seen along cracks and possible cleavage planes in the zircon.

Figure 7: Chondrite normalized (McDonough and Sun, 1995) plots of Y + HREE from altered and unaltered areas of zircon in experiments (**a**) ZF-5 ($Na_2Si_2O_5$ + H_2O), (**b**) ZF-9 (2N NaOH), (**c**) ZF-16 (NaF + H_2O), and (**d**) ZF-40 (NaF + H_2O) (see Tables 2 and 3; Table S4).

Metasomatic alteration of zircon at lower crustal P-T conditions utilizing alkali- and F-bearing fluids: trace element incorporation, depletion, and resetting the zircon geochronometer

Daniel E. Harlov[1,2,3*], Robert Anczkiewicz[4], and Daniel J. Dunkley[5,6]

[1]Deutsches GeoForschungsZentrum-GFZ, Telegrafenberg, 14473 Potsdam, Germany

[2]School of Earth Resources, China University of Geosciences, Wuhan 430074, China

[3]Department of Geology, University of Johannesburg P.O. Box 524, Auckland Park, 2006 South Africa

[4]Institute of Geological Sciences, Polish Academy of Sciences, Krakow Research Centre, Senacka 1, 31-002 Krakow, Poland

[5]Department of Polar and Marine Research, Institute of Geophysics, Polish Academy of Sciences Księcia Janusza 64, PL-01452 Warsaw, Poland

[6]National Institute of Polar Research, 3-10 Midori-cho, Tachikawa-shi, Tokyo-to, 190-8518 Japan

*dharlov@gfz-potsdam.de

ABSTRACT

Natural alteration of zircon takes place in melts or fluids either via dissolution coupled with overgrowth or via a coupled dissolution-reprecipitation process. The latter results in the zircon being partially or totally replaced by new, compositionally re-equilibrated zircon or a new mineral phase or both. In this study, fragments (50 – 300 μm) from a large, inclusion-free, clear, 520 to 530 Ma euhedral zircon with light radiation damage from a nepheline syenite pegmatite, Seiland Igneous Province, northern Norway, were experimentally reacted in 20 mg batches with 5 mg of

ThO_2 + $ThSiO_2$ + SiO_2 and a series of alkali-bearing fluids in sealed Pt capsules at 900 °C and 1000 MPa for 6 to 11 days in the piston cylinder press using a CaF_2 setup with a cylindrical graphite oven. ThO_2 + $ThSiO_2$ + SiO_2 was present at the end of the experiment. In experiments involving H_2O, H_2O + NaCl, H_2O + KCl, and 2N KOH, no reaction textures formed other than a slight dissolution of the zircon grain fragments. Experiments involving 2N NaOH, $Na_2Si_2O_5$ + H_2O, and NaF + H_2O resulted in zircon reaction textures with varying degrees of intensity, which took the form of partial replacement by compositionally modified zircon via a coupled dissolution-reprecipitation process. In the NaF + H_2O experiment some overgrowth also occurred. Altered zircon is separated by sharp compositional boundaries from unaltered zircon. Secondary ion mass spectrometry (SIMS) and laser ablation inductively coupled plasma mass spectrometry (LA-ICP-MS) analysis indicates that, relative to the unaltered zircon, the altered zircon is strongly enriched in Th, and heavily to moderately depleted in U and (Y+REE). In all the experiments, ^{206}Pb (3 to 5 ppm in unaltered zircon) is depleted in the altered zircon to below the SIMS detection limit and to at or below the LA-ICP-MS detection limit. Hafnium and Ti concentrations in the altered zircon retained the same approximate value (within error) as the original zircon. The results from these experiments demonstrate that zircon can be compositionally modified by alkali-bearing and alkali-F-bearing fluids via a coupled dissolution-reprecipitation process. Near to total loss of radiogenic Pb via such processes under high-grade conditions resets the internal zircon geochronometer. Although the end result is the same as with zircon overgrowth, i.e. the production of new generation zircon at the time of a metasomatic/metasomatic event, such replacement processes can explain incomplete isotopic ‘resetting’; inclusion production through unmixing of solid solutions in metastable zircon compositions; and ‘ghost’ textures that preserve initial growth features but with isotopic disturbance. Diagnostic replacement features produced in experiments, such as interface geometries between altered and unaltered zircon, provide markers of the mechanism and aid in zircon interpretation. A major implication from this study is that if zircon with low radiation damage can be metasomatically altered under high-grade conditions this would have important

consequences with respect to zircons presumed role as an impregnable container for mineral inclusions. Namely the mineral inclusions contained within zircon could also be altered, reset as a geochronometer, or even replaced by another mineral.

Keywords: zircon, Th, U, Pb, REE, petrochronology, coupled dissolution-reprecipitation, alkali-bearing fluids, experimental petrology

1. Introduction

In nature zircon is one of the principal accessory minerals used for the dating of geologic processes. Its chemically and mineralogically robust nature allows it to survive its igneous origins and be re-incorporated into either successive igneous protoliths, through melting of zircon-bearing source rocks, or into sedimentary protoliths, as detritus. Zircon can also survive metamorphism, metasomatism, and/or partial melting of the host rock. However, such survival is typically partial. The cores of the zircon grain tend to preserve its origins whereas the rims and replacement textures can record changes wrought during diagenesis, metasomatism, metamorphism, and re-incorporation into a magma (e.g. Harlov et al., 2022).

Zircon is a principal host for U, Th, Hf, Y, and HREEs in various sedimentary, metamorphic, and igneous rocks, and as such can contain a significant fraction of the whole rock abundance of these elements depending on the presence or lack of other minerals such as monazite, xenotime, allanite, apatite, and garnet. Despite its reputation as a refractory mineral, zircon can interact with diverse fluids and/or melts under a range of crustal P-T conditions. For example, the chemical stability of metamict zircon, radiation-damaged zircon, and synthetic (pristine) zircon with respect to various fluids has been explored experimentally as well as speculated upon in a series of studies of natural examples utilizing a variety of analytical techniques, as summarized in Geisler et al. (2007); see also Pidgeon et al. (1966), Rizvanova et al. (2000), Geisler et al. (2002, 2003), Tomaschek (2004, 2010), Lenting et al. (2010), and Lewerentz et al. (2019). Both experimentally

and in nature, compared to pristine zircon or zircon with a low degree of radiation damage, metamict zircon and zircon with a high degree of radiation damage is highly susceptible to fluid-assisted alteration down to relatively low P-T conditions (e.g., 175 °C and 250 bars) (Geisler et al., 2007).

In addition to metamict and radiation damaged zircon, reaction textures, presumed to be produced by fluids or melts, can also be seen in zircons with a low degree of radiation damage from both igneous and high-grade metamorphic rocks under cathodoluminescence (CL) imaging. Examples include zircons from a ca. 983 Ma anorthosite, Eastern Ghats Mobile Belt, India (Chatterjee et al., 2008); orthopyroxene-bearing granulite-facies granitoids (charnockites) from the Shevaroy Massif, southern India (Harlov et al., 2022); polymetamorphic migmatites, Valle d'Arbedo, Switzerland (Vonlanthen et al., 2012); granulite-facies meta-granitoids, Queensland, Australia (Hoskin and Black, 2000); and granitic gneisses in a contact aureole associated with the Rogaland anorthite-norite intrusive complex, southern Norway (Möller et al., 2002). Here CL-bright or CL-dark areas of apparent alteration overprint the original magmatic zoning (Fig. 1). The irregular and/or lobate shapes of these altered areas, which extend inward into the zircon from the grain rim, are difficult to ascribe to overgrowth of either the original zircon grain or partially dissolved zircon grain, but rather resemble the partial replacement textures in monazite that have been shown to be the result of fluid-induced coupled dissolution-reprecipitation processes as opposed to overgrowth (Harlov et al., 2011).

In this study, fragments of an inclusion-free, faintly banded zircon (CL imaging) with light radiation damage from the Seiland Igneous Province, northern Norway (Fig. 2) are used in a series of piston cylinder metasomatism experiments involving both pure H_2O and a variety of alkali-bearing solutions at 900 °C and 1000 MPa. A $ThSiO_4$ + ThO_2 + SiO_2 mix was added to all of the experiments with the goal of seeing whether or not Th could be metasomatically incorporated into the zircon crystal lattice replacing Zr utilizing reactive fluids. After quench and extraction, the reacted zircon grain fragments are then mounted, polished to cross section, and evaluated using

high-contrast backscattered electron (BSE) imaging, CL imaging, transmission electron microscopic (TEM) imaging, electron microprobe (EMP) analysis, sensitive high-resolution ion microprobe (SHRIMP) analysis, and laser ablation inductively coupled plasma mass spectrometry (LA-ICP-MS) analysis. The results from the experimentally reacted zircons are then compared with metasomatically altered zircons from nature and the reaction textures are interpreted chemically, physically, and from a petrochronological perspective.

2. Experimental and Analytical Procedures

2.1 Experimental protocol

Experiments were run at 900 °C and 1000 MPa using the two piston cylinder apparatus as described by Johannes et al. (1971) and Johannes (1973) and are summarized in Table 1. The zircon chosen for the experiments was obtained from the Natural History Museum at the University of Oslo, Oslo, Norway. It consists of a large (2 cm), transparent, inclusion-free, light brownish, euhedral crystal fragment from a nepheline syenite pegmatite located in the Seiland Magmatic Province, northern Norway (523 ± 2 to 531 ± 2 Ma; Pedersen et al., 1989). A fragment of this crystal was broken up into 50 to 300 μm size irregular grains. The transparent, inclusion-free, lightly brown-pink grain fragments were washed in ethanol in an ultrasonic bath. Size sorting was not done. High contrast BSE and CL imaging reveal that the grains are totally texture-free except for a very faint magmatic zoning (Fig. 2).

Solids in the experimental charge consisted of 20 mg of zircon, 5 mg of a $ThSiO_4$ + ThO_2 + SiO_2 mix, and 5 mg of fluid (Table 1). Reactants in the experimental charge included doubled distilled nanopore H_2O, NaCl + H_2O, KCl + H_2O, 2N NaOH, 2N KOH, $Na_2Si_2O_5$ + H_2O, and NaF + H_2O. All chemicals used were spec pure to 99.99% or better. The experimental charge was placed in a 3 mm wide, 1 cm long, tempered (1000 °C) Pt capsule, which was arc-welded shut and placed vertically, four at a time, in a CaF_2 setup with a cylindrical graphite oven (Fig. 3). The capsules were separated from each other by thin sheets of biotite. The presence of a graphite oven under the

airtight conditions of the experiment implies that the system/experiments, at least in theory, should have been buffered to graphite-CO-CO_2 once the oven was heated to 900 °C. The thermocouple tip was placed such that it reached halfway up alongside the Pt capsules (Fig. 3). The temperature differential along the capsules was approximately 40 °C with either capsule end at 860 °C compared to the sweet spot at the center of the capsules at the measured 900 °C. The pressure measured during the experiment was corrected for friction due to the CaF_2 pressure medium. Non-isobaric quench was achieved within 20 to 30 seconds by turning off the current.

After each experiment, the Pt capsule was cleaned, weighed, and punctured. The Pt capsules were then dried at 105 °C for several hours, and weighed again to determine fluid loss. Due to the very small amounts of fluid used in the experiments (5 mg), accurate trace element analysis of the fluid was not possible. The reacted charge was then carefully removed from the Pt capsule with as little mechanical disturbance as possible. The charge was then mounted and polished down to cross section in an epoxy grain mount.

2.2 Scanning electron microscope (SEM)

Experimental charges were first evaluated using high contrast BSE and CL imaging on a JEOL JSM–5900LV Scanning Electron Microscope (SEM) equipped with a Gatan MiniCL detector and JEOL SmileStation stage automation and image-capture software at the National Institute for Polar Research (NIPR), Tachikawa-shi, Tokyo-to, Japan.

2.3 Electron probe microanalysis (EPMA)

Electron probe microanalysis (EPMA) of zircon was carried out using the JEOL electron hyperprobe with field emission gun at the GeoForschungsZentrum (GFZ) Potsdam using an accelerating voltage of 15 kV and beam current of 15 nA. Individual spot analyses were made using a focused electron beam with a diameter of 1 micron. Elements analyzed for in zircon included P, Si, Ti, Zr, Hf, Th, U, Y, Gd, Tb, Dy, Ho, Er, Yb, Lu, Ca, Pb, and Na, with counting

times of 20 to 120 seconds depending on the relative amount of the element. Standards for the REE were taken from synthetic REE phosphates prepared by Jarosewich and Boatner (1991). The remaining standards were taken from both the CAMECA and Smithsonian standard sets (Jarosewich et al., 1980). The full EMP analysis data set is contained in ~~Supplementary Material~~ Table S1.

2.4 Sensitive high-resolution ion microprobe (SHRIMP)

2.4.1 Zircon U-Th-Pb measurement

Mounted zircon grains were cleaned to eliminate surface contamination by common Pb, and coated with 100 Angstroms of high-purity gold. Mounts were imaged at high resolution by CL and BSE with a JEOL JSM–5900LV Scanning Electron Microscope (SEM) equipped with a Gatan MiniCL detector and JEOL SmileStation stage automation and image-capture software, at NIPR, Tachikawa-shi, Tokyo-to, Japan.

Spots were carefully chosen from SEM imaging for Th, U, and Pb analysis during multiple sessions by a SHRIMP-II at NIPR, using a primary O_2-ion beam with a typical sample surface current of 4 to 7 nA to produce 25 to 30 µm long, flat-floored oval pits. Secondary ionization was measured on a single electron multiplier on mass stations 196 (Zr_2O) through to 254 (UO), with a mass resolution of > 5000 for $^{238}U^{16}O$ and a sensitivity on ^{206}Pb of 17 to 20 cps per ppm per nA of primary current. Mass stations were measured through 5 to 6 cycles, with typical count times of 10 s per cycle for ^{204}Pb, background (at 204.04 amu) and ^{206}Pb, and 20s for ^{207}Pb. Reduction of raw data for standards and samples was performed using the SQUID v.1.12a (Ludwig, 2001), and Isoplot v.3.71 (Ludwig, 2003) add-ins for Microsoft Excel 2003. Abundance of U was calibrated against in-house reference zircon YBr157 (580 ppm U, as estimated by TIMS; provided by Allen Kennedy of the John de Laeter Centre, Curtin University of Technology, Western Australia, Australia). Corrections for common Pb on U/Pb values and ages were done with the common Pb estimated from ^{204}Pb counts and the Stacey and Kramers (1975) common Pb model for the

approximate U-Pb age for each analysis. (Pb/U)/(UO/U)^2 values were calibrated against measurements on reference zircon TEMORA-2 (417 Ma; Black et al., 2004). Zircon SHRIMP mean U-Th-Pb data for the reacted zircons listed in Table 1 is contained in Table 2. The full SHRIMP analytical U-Th-Pb zircon data set is contained in ~~Supplementary Material~~ Table S2.

2.4.2 Zircon Y+REE analysis

Yttrium, REEs, and Hf contents were estimated for a subset of U-Th-Pb isotopic analyses by re-analyzing the same spots (Table 2). Considering the small penetration depth (< 3 micron) of the SHRIMP analytical spots, and the lack of strong chemical zoning ion in the starting material these contents are considered to be equivalent to those in zircon analyzed for U-Th-Pb. Spot sizes and mass resolutions were the same as for age analyses, with each station measured for 10 s through 6 cycles. To minimize the interference of LREE-MREE oxide peaks on MREE-HREE and Hf measurements, energy filtering was applied to reduce ^{180}Hf to 10% of the unfiltered signal. This reduces potential REEO$^+$ interference to less than 1% of the unfiltered signals. Counts were normalized against ^{92}Zr from the NIST610 standard glass, and compared periodically against published values for zircon reference material 91500 (Wiedenbeck et al., 2004; Iizuka and Hirata, 2004). All estimates were within 10% of published values. Zircon SHRIMP mean REE data for the reacted zircons listed in Table 1 is contained in Table 2. The full SHRIMP analytical zircon REE data set is contained in ~~Supplementary Material~~ Table S3. Chondrite-normalized REE plots of the SHRIMP REE data are contained in ~~Supplementary Material~~ Figure S1.

2.5 Laser ablation inductively coupled plasma mass spectrometry (LA-ICP-MS)

Trace element abundances in zircon were measured at the Institute of Geological Sciences, Polish Academy of Sciences, Kraków Research Centre, Krakow, Poland using an ArF excimer laser-ablation system RESOlution M50 by Resonetics coupled with a quadrupole ICP-MS XSeriesII by FisherScientific. Ablation took place in a double volume Laurine technology cell in pure He (flow

rate of 0.9 L/min), for which the Ar nebuliser gas (flow rate of 0.5 – 0.55 L/min) was mixed downstream from the sample cell. After passing through a signal-smoothing manifold, the analyte was delivered to the ICP source. A small addition of nitrogen (0.005 – 0.008 L/min) was used to enhance the sensitivity of the ICP-MS. The oxide to metal ratio $^{248}ThO/^{232}Th$ was kept below 0.5 %. Analyses were performed using a rotating rectangular slit with a length of 50 µm and a width of 8 and 16 µm. An energy density of 4 to 5 J/cm^2 at a repetition rate of 5 Hz was applied. Twenty seconds of gas blank was measured prior to each 30 s ablation, which was followed by 30 s washout time. Sample runs were bracketed by measurements of the NIST 612 glass (Jochum et al., 2011). The zircon reference material 91500 (Wiedenbeck et al., 2004; Iizuka and Hirata, 2004) was frequently measured as a secondary standard along with the unknowns. The ZrO_2 content from previously acquired electron microprobe analyses of the Seiland zircon (ZrO_2 = 66.65; SiO_2 = 32.20; HfO_2 = 0.70) was used as an internal standard (~~Supplementary Material~~ Table S1). Data processing was performed using the Glitter 4.0 software from Macquarie University, Australia (Griffin et al., 2008). Zircon LA-ICP-MS mean U-Th-Pb and REE analyses for the reacted zircons listed in Table 1 is contained in Table 3. The full LA-ICP-MS analytical U-Th-Pb and REE zircon data set is contained in ~~Supplementary Material~~ Table S4.

2.6 Transmission electron microscopy (TEM)

Reacted zircon grains, suitable for TEM investigation, were first selected using BSE and SEM images. Sampling was accomplished by using focused ion beam (FIB) milling (Wirth, 2004, 2009). FIB preparation was conducted under ultra-high vacuum conditions in an oil-free vacuum system using a FEI FIB200 instrument at the GeoForschungsZentrum Potsdam. TEM-ready foils of approximately 15 x 8 x 0.15 µm representing cross sections perpendicular to and across the reaction front (separating the altered and unaltered zircon) were sputtered directly from the zircon grain in the epoxy grain mount using a 30 kV Ga-ion beam. The TEM foil was protected from sputtering by the Ga-ion beam by a 1 µm thick, Pt layer deposited using a high-purity organic Pt gas ($C_9H_{16}Pt$,

99.9 %), which decomposes under the Ga-ion beam. Once cut, the TEM foils were placed on a perforated carbon film, which was placed on a copper grid. Carbon coating to prevent charging in the TEM was not applied.

TEM on the zircon foils was carried out in a TECNAI F20 XTwin instrument operated at 200 kV and equipped with a FEG electron source. The TEM is equipped with a Gatan imaging filter (GIF Tridiem), a Fishione high-angle annular dark field detector (HAADF), and an EDAX X-ray analyzer with an ultrathin window. TEM bright field images (HREM) were acquired as energy-filtered images applying a 10 eV window to the zero-loss peak.

3. Results

All experiments were run at 900 °C and 1000 MPa over periods of 144 to 192 hours (6 – 8 days). Whereas, the zircon grain fragments were a light pinkish brown before the experiment, at quench the reacted zircon grain fragments were colorless and transparent, which suggests that any radiation damage in the zircon had been healed. This is supported by a variety of annealing experiments at comparable or lower temperatures and/or pressures (cf. Nasdala et al., 2001, 2002; Montario et al., 2008; Ginster et al., 2019; Herrmann et al., 2021; Ende et al., 2021; Härtel et al., 2022). Of the eight experimental runs reported here and listed in Table 1, in those experiments involving pure H_2O, NaCl + H_2O, KCl + H_2O, and 2N KOH, the zircon did not react with the fluid, other than showing a little dissolution along the grain fragment edge. In contrast, zircon in experiments involving $Na_2Si_2O_5$ + H_2O (Fig. 4), 2N NaOH (Fig. 5), and NaF + H_2O (2 experiments; Table 1, Fig. 6) developed reaction textures under CL imaging to varying degrees. In each of these experiments, due to the relatively large amount of the $ThSiO_4$ + ThO_2 + SiO_2 mix added (Table 1), all three phases persisted to the end of the experiment and were visible in the reacted charge.

While not obvious in high contrast BSE images, under CL imaging the altered areas in these four experimental runs appear lighter (CL-light) than the unaltered areas (CL-dark). CL-light areas are separated from CL-dark areas by sharp boundaries. In the experiments involving $Na_2Si_2O_5$ +

H_2O (ZF-5; Fig. 4) and 2N NaOH (ZF-9; Fig. 5), the reaction textures are considerably less extensive than in runs involving NaF + H_2O (ZF-16, ZF-40; Fig. 6). In the case of run ZF-9, only two zircon fragments with a reaction texture were found amongst 30 grain fragments exposed in the polished mount, which makes up about half of the total experimental product. In the case of ZF-5, about half of the grains in the grain mount had reaction textures. In contrast, in the NaF + H_2O experiment (ZF-16, ZF-40), all the zircon grains developed reaction textures ranging from slight to extensive. In runs ZF-5 and ZF-9, a lack of crystal face formation and the preservation of irregular grain fragment boundaries would suggest that the reaction textures are due to the replacement of the original zircon by altered zircon. In runs ZF-16 and ZF-40, the development of new crystal faces as a product of overgrowth is evident on some of the grains (e.g. Fig. 6a). However, reaction textures have also developed that are lobate and convex inwards, away from edges of zircon grain regardless of whether they have overgrowths or not (e.g. Figs. 6a,c,d). A second type of reaction texture occurs along cracks and possible cleavage planes inside of the zircon grains, which extends outwards from the crack into the zircon (Figs. 6e,f). There is a general lack of crystal face formation despite the fact that, due to the high ratio of fluid to zircon grain fragments by mass (Table 1), each individual grain was totally surrounded by fluid during the experiment and, hence, not in direct contact with any of the other grains unless it was overgrown by a neighboring grain (e.g. Fig. 6a).

TEM bright field images of foils sampled across the reaction front, as defined by CL imagery, in zircon grains from runs ZF-5 (Figs. 4a,b), ZF-9 (Figs. 5a,b), and ZF-16 (Figs. 6a,b), show no differences in texture on the sub-micron scale between the altered and unaltered areas in the zircon, no mineral inclusions, nor any evidence of a boundary or reaction front between the unaltered and altered zircon.

In general, both SHRIMP and LA-ICP-MS spot analyses indicate that the CL-light altered areas are moderately to heavily depleted in U and Y + HREE and enriched in Th relative to the CL-dark unaltered areas of the zircon grains, which retain the trace element abundances of the original zircon grain (Tables 2 and 3; Fig. 7; ~~Supplementary Material~~ Fig. S1; ~~and~~ Tables S2, S3, and S~~–~~4).

The low Th and U contents in the original Seiland zircon would imply that the amount of radiation damage to the crystallographic lattice should be relatively minor after some 520 to 530 Ma (Table 3; ~~Supplementary Material~~ Tables S2 and S4). One exception was ZF-5 ($Na_2Si_2O_5$ + H_2O). Here Gd showed no depletion within the altered areas (Fig. 7a, ~~Supplementary Material~~ Fig.~~ure~~ S1; Tables 3 and 4). In contrast, altered areas in all the experiments are heavily depleted in Pb to or below the detection limit in both the SHRIMP and LA-ICP-MS analytical data, whereas Hf and Ti show little difference in their abundances (within analytical error) between the altered and unaltered areas in the zircon (Tables 2 and 3; ~~Supplementary Material~~ Tables S3 and S4).

4. Discussion

4.1 Formation of reaction textures in zircon

A series of previous studies have focused on the experimental alteration of zircon, though most of these have involved metamict or zircon with a high degree of radiation damage under temperatures and pressures lower than the ones considered in this study (Pidgeon et al., 1966; Geisler et al., 2001a,b, 2002, 2003, 2004, 2007; Rizvanova et al., 2000, 2007; Lenting et al., 2010; Lewerentz et al., 2019). In general, these experiments have involved a variety of fluids (H_2O, HCl, $Ca(OH)_2$ + H_2O, $CaCl_2$ + H_2O, and $AlCl_3$ + H_2O) over a broad range of temperatures (200 – 700 °C) and pressures (100 – 500 MPa). The zircon in these experiments generally shows a high degree of reactivity during the experiment due to the large amount of chemical potential energy stored in the disordered, amorphous areas in the zircon or in the radiation-damaged zircon crystallographic lattice (see discussion in Geisler et al., 2007). Other experiments at high P-T have focused on annealing of zircon in restricted chemical systems (Morales et al., 2022), the relationship between zircon and baddeleyite as a function of the Ca and Si activity in fluids (Lewerentz et al., 2019), or on the dissolution of zircon in a variety of silicate melts (Borisov and Aranovich, 2019; Baker et al., 2002; Schmidt et al., 2013) and in a series of fluids (Schmidt et al., 2006; Newton et al., 2010; Ayers et al., 2012; Wilke et al., 2012; Bernini et al., 2013; Ayers and Peters, 2018).

In this study, utilizing pressures and temperatures that are normally characteristic of the lower crust/lithospheric mantle, the goal was to partially alter a natural zircon with a low degree of radiation damage metasomatically while at the same time incorporating Th in the altered areas. The reaction textures produced in the experimentally metasomatized zircon show a sharp contrast, both texturally and compositionally (trace elements), between the altered (CL-bright) and unaltered (CL-dark) zircon (Figs. 4, 5, and 6). The lobate intergrowths of altered zircon into the unaltered zircon as seen in Figures 6a, 6c, and 6d can be argued as not being a product of overgrowth, but rather a product of mineral replacement (see comments above). Similar textures, both lobate and otherwise, have been recognized in metasomatically altered monazite (cf. Harlov et al., 2011), xenotime (Harlov and Wirth, 2012), and apatite (Harlov et al., 2002, 2003, 2005) both experimentally and from nature, and have been interpreted as partial replacement textures due to a coupled dissolution-reprecipitation process (Putnis, 2002, 2009; Putnis et al., 2005; Putnis and Putnis, 2007; Putnis and Austrheim, 2010, 2013; Altree-Williams et al., 2015). This is especially obvious in Figures 4c, 6e, and 6f where alteration occurs along cracks and possible cleavage planes within the zircon grains as partial replacement textures extending into the zircon, similar to that seen in partial replacement textures involving experimental replacement of monazite by huttonite ($ThSiO_4$) (cf. Harlov et al., 2007, their figure 2h). During coupled dissolution-reprecipitation, the original zircon is dissolved in the presence of these alkali-bearing fluids while simultaneously being replaced by new zircon that compositionally is in thermodynamic equilibration with the fluid chemistry under the particular P-T conditions of the system. During this process, the new zircon uses the original zircon as a crystallographic template for purposes of nucleation and subsequent growth/replacement. In essence coupled dissolution-reprecipitation is the basis for mineral pseudomorphism, and is a commonly observed process in nature for many minerals. It is also the principal process by which fossilization of organic material, such as bone and wood, occurs.

In minerals, the process of coupled dissolution-reprecipitation has been shown to occur along a very thin (10 nm wide or less) fluid-filled reaction front between the original dissolving

mineral and the newly growing mineral (Putnis, 2002, 2009; Altree-Williams et al., 2015). This reaction front is physically connected to the fluid surrounding the mineral grain via an actively evolving, non-static, interconnected porosity prevalent throughout the newly grown mineral phase. This allows for active fluid-aided mass transfer between the fluid along the reaction front and the fluid surrounding the grain during the replacement process. Porosity formation can result from a variety of causes such as differences in the molar volume between the original and replacement phase or differences in solubility between the two phases (Putnis, 2009). Once this replacement process stops due to changing P-T-X conditions in an open fluid-mineral system or, in the case of a closed system, due to limited amounts of the reactive fluid (e.g. the experiments in this study), the reaction front will cease to advance and the altered areas of the mineral will begin to recrystallize such that the original interconnected porosity will evolve into isolated nano- and micron-size fluid inclusions often along with mineral inclusions, both those genetically derived from the host mineral and those originating from minerals outside of the host mineral (Putnis, 2002, 2009; Harlov et al., 2005, 2011; Harlov and Wirth, 2012; Harlov et al., 2016).

As can be seen in Figures 4b, 5c, and 6b, for each of the alkali-bearing fluid-zircon metasomatism experiments, neither a remnant porosity nor mineral inclusions remain in the altered areas of the zircon under CL imaging nor in TEM foils taken perpendicular to the reaction front, which includes both altered zircon and unaltered zircon. Here the reaction front, so clearly visible under CL imaging, is not visible in the TEM foils, i.e. the altered zircon appears texturally indistinguishable from the unaltered zircon (cf. Figs. 4b, 5b, and 6b). This is not what is seen in the reaction textures and accompanying TEM foils taken across reaction fronts in experimentally metasomatized fluorapatite (Harlov et al., 2005), monazite (Harlov et al., 2011), and xenotime (Harlov et al., 2012) from experiments done under the same approximate P-T conditions. It is also not seen in experimentally metasomatized metamict or radiation-damaged zircon (Geisler et al., 2007), nor in metamict or radiation-damaged zircon from nature (Geisler et al., 2002, 2003, 2007). In all of these cases the metasomatically altered areas are characterized by numerous fluid

inclusions and mineral inclusions, such as $ThSiO_4$, $USiO_4$, ThO_2, UO_2, ZrO_2, xenotime, feldspar, quartz, etc..

One explanation for this striking difference in zircon textures is that the alteration textures seen in Figures 4, 5, and 6 appear to be specific to zircon with low amounts of radiation damage, characteristic of the 520 to 530 Ma Seiland zircon, the high P-T conditions of the experiments, and the reactivity of the alkali-bearing and F-bearing fluid chemistry of the system. Total elimination of the porosity during the course of the experiment, after growth of the altered area had stopped, could be due to a rapid coarsening effect, which would be consistent with attaining textural equilibration driven by reduction in the surface area as defined by the interior surface area of the pores. Hence, the original porosity, which was transient to begin with, would have totally disappeared as textural equilibration was achieved, and in this particular case achieved rather quickly during the course of the experiment. Similar phenomena have been observed in the KBr-KCl-H_2O replacement experiments of Putnis et al. (2005). Rapid disappearance of the porosity would have also discouraged mineral inclusion formation since the pores normally act as nucleation sites for inclusions in the altered/reacted areas (see discussion in Harlov et al., 2005). What overgrowth that did occur was also totally recrystallized as per the above mechanism eliminating any porosity that might have formed during crystal growth outwards. The sharp compositional boundary seen between the altered zircon and unaltered zircon under CL imaging would indicate that element diffusion across the boundary was negligible at 900 °C and 1000 MPa over the course of the experiment. This observation agrees with the U, Th, and Hf diffusion experiments of Cherniak et al. (1997a) and REE diffusion experiments of Cherniak et al. (1997b), both of which indicate very slow diffusion rates at high temperatures for these elements in zircon.

Comparison of the reaction textures resulting from the experiments (Figs. 4 – 6) with similar textures in natural zircons in Figure 1 support the proposition that high-grade, high pH, alkali-bearing/F-bearing fluids could have been responsible for them. The examples provided in Figure 1 are found in both metamorphic and igneous rocks in a fluid-rich environment with broadly granitoid

and hence alkali-rich compositions or else are associated with such rocks. These observations are supported by Aranovich et al. (2017) who make a strong case for alkali-bearing fluids causing partial to total alteration of zircon grains in gabbroids and plagiogranites from the Mid-Atlantic Ridge. In another example, zircons from a leucocratic granite of the Weondong region of South Korea show four types of partial metasomatic alteration, which the authors attribute to the action of F-rich fluids during post-magmatic alteration (Park et al., 2016; their figures 3 and 5). The textures of these metasomatised zircon grains broadly mimic some of the reaction textures obtained in the NaF-fluid experiments (Fig. 6).

4.2 Alteration of the zircon trace element chemistry

Relative to the original unaltered Seiland zircon, the altered areas in the zircon are significantly enriched in Th, significantly depleted in U, moderately to strongly depleted in Y + HREE, and nearly to totally depleted in Pb to within the detection limit of both SIMS and LA-ICP-MS. In contrast, there is little or no change in the Hf or Ti content within the measurement precision (Tables 2 and 3; Fig. 7). These abundances contrast with the fluids used in the experiments, which were saturated in Th + Si, and totally devoid of U, Pb, Y+REE, Ti, and Hf (Table 1). .

In the zircon crystallographic lattice, U^{4+}, Th^{4+}, and Hf^{4+} are conventionally considered to substitute for Zr^{4+} on the 8-fold Zr site (Finch and Hanchar, 2003; Hoskin and Schaltegger, 2003). While, Th and U have a limited solid solution with zircon as tetragonal thorite ($ThSiO_4$), and tetragonal coffinite ($USiO_4$), respectively (Ushakov et al., 1999), Hf has a complete solid solution with zircon as tetragonal hafnon ($HfSiO_4$) (Speer and Cooper, 1982). This is due to the fact that on the 8-fold Zr site Hf^{4+} (0.83 Å) can completely substitute for Zr^{4+} (0.84 Å) (effective ionic radii; Shannon, 1976; Harley and Kelly, 2007). In contrast, the relatively larger 8-fold ionic radii of U^{4+} (0.86 Å) and Th^{4+} (1.05 Å) (Shannon, 1976; Harley and Kelly, 2007), compared to 8-fold Zr^{4+} (0.84 Å), would explain their relatively limited solid solution in zircon. It would also explain as to why U^{4+} was so easily removed and Th^{4+} only incorporated in limited amounts during each of the

metasomatism experiments despite the fluid being supersaturated with Th (Table 3; ~~Supplementary Material~~ Tables S2 and S4).

Yttrium and the REE are generally thought to be incorporated into zircon via a xenotime-type coupled substitution or:

$$^{VIII}(Y+REE)^{3+} + {}^{IV}P^{5+} = {}^{VIII}Zr^{4+} + {}^{IV}Si^{4+} \quad (1)$$

(Finch and Hanchar, 2003; Hoskin and Schaltegger, 2003) with $(Y+REE)^{3+}$ going on the 8-fold Zr site and P^{5+} (0.17 Å) on the 4-fold Si^{4+} (0.26 Å) site (effective ionic radii; Shannon, 1976). Other possible coupled substitutions for (Y+REE) in zircon which have been described in the literature include:

$$Li^{+}_{(interstitial)} + {}^{VIII}(Y+REE)^{3+} = {}^{VIII}Zr^{4+} \quad (2)$$

(Finch et al., 2001; Wang and Trail, 2022), and:

$$H^{+}_{(interstitial)} + {}^{VIII}(Y+REE)^{3+} = {}^{VIII}Zr^{4+} \quad (3)$$

(Trail et al., 2016) where Li and H substitute on interstitial sites in the zircon structure (Finch and Hanchar, 2003). In all of these cases, 8-fold $(Y + HREE)^{3+}$ (1.019, 1.079 – 0.977 Å) are strongly preferred over the 8-fold $LREE^{3+}$ (1.160 – 1.109 Å) due to their better fit on the 8-fold Zr (0.84 Å) site (Hoskin and Schaltegger, 2003; Shannon, 1976).

From the LA-ICP-MS data in ~~Supplementary Material~~ Table S4, $(Y+HREE)^{3+}$ plus the approximate value for P^{5+} when plotted vs. $Zr^{4+} + Si^{4+}$ for both unaltered and altered zircon in each of the experiments show an approximate linear relationship with a positive shallow slope. This indicates that an additional coupled substitution mechanism must have been responsible for Y+HREE incorporation in both the altered and unaltered zircon. These additional mechanisms could have included coupled substitutions (2) and/or (3), each to varying degrees, though this must be treated as speculation since neither Li nor H^{+} were measured.

The observation that Ti was not depleted in the altered areas (Table 3) is more curious considering that the alkali-bearing solutions in each of the experiments were not buffered by rutile, i.e. TiO_2, or some other Ti-rich mineral such as ilmenite or titanite; though each of the solutions was

buffered to an SiO_2 activity of 1 due to the presence of free SiO_2 in the capsule at the end of the experiment. In zircon, relatively limited amounts of Ti, as $^{IV}Ti^{4+}$ (0.42 Å) are believed to substitute for $^{IV}Si^{4+}$ (0.26 Å) (effective ionic radii; Shannon, 1976) on the tetrahedral site with the amount of Ti present increasing as a function of increasing temperature for a system nominally buffered at a constant TiO_2 activity (Watson and Harrison, 2005; Watson et al., 2006; Ferry and Watson, 2007; Harley and Kelly, 2007; Tailby et al., 2011). The fact that Ti remained in the altered areas of the zircon at 900 °C and 1000 MPa in a Ti-free system (Table 1), as opposed to selectively partitioning into the solution, would suggest that for minor amounts of Ti, the partitioning coefficients for NaF-, NaOH-, and $Na_2Si_2O_5$-bearing solutions apparently favor Ti remaining on the tetrahedral site in zircon at the P-T of the experiments. Such an observation could have implications for the Ti-in-zircon geothermometer in alkali fluid-bearing systems whether they are buffered with respect to TiO_2 or not (cf. Ferry and Watson, 2007).

Lead appears to be broadly incompatible in the zircon structure with respect to substitution on either the tetrahedral Si site or the octahedral Zr site due to its much larger size, i.e. $^{IV}Pb^{4+}$ (0.65 Å) vs. $^{IV}Si^{4+}$ (0.26 Å) and $^{VIII}Pb^{4+}$ (0.94 Å) vs. $^{VIII}Zr^{4+}$ (0.84 Å) (effective ionic radii; Shannon, 1976; Watson et al., 1997; Mezger and Krogstad, 1997; Geisler et al., 2003; Utsunomiya et al., 2004; Kogawa et al., 2012). This assumes that Pb would occur as Pb^{4+} in the zircon structure, which would seem highly unlikely assuming that the experiments were presumably buffered to graphite-CO_2 (see above). If Pb in the original, unaltered zircon existed only as Pb^{2+}, in addition to there being a question of charge balance, the misfit of Pb on both the Si and Zr sites becomes even greater, i.e. 0.98 vs. 0.26 Å and 1.29 vs. 0.84 Å, respectively. This would imply that the only Pb present in the original zircon should be from the radioactive decay of U, Th, and their short-lived daughter isotopes in the form of small accumulations in amorphous radiation-damaged domains and/or along cleavage planes, or as nano-inclusions in annealed zircon (Geisler et al., 2003; Nasdala et al., 2005; Kogawa et al., 2012; Seydoux-Guillaume et al., 2015; Valley et al., 2014, 2015; Lyon et al., 2019). A similar case has been made for Pb accumulation in monazite (Fougerouse et al.,

2018). The fact that Pb is so readily removed from the altered areas of the zircon to the extent of being at or below the detection limits of both LA-ICP-MS and SIMS implies that Pb, at least in trace amounts, is apparently highly soluble in NaF-, NaOH-, and $Na_2Si_2O_5$-bearing fluids at 900 °C and 1000 MPa most likely due to complexing with either OH^- or F^- in solution (Bottari and Ciavatta, 1965; Perera et al., 2001).

The addition of Th, loss of U, and near to total loss of Pb in the altered areas of the zircon would imply that the U-Th-Pb geochronometer has been near to totally reset compared to the unaltered areas. This obviously has major implications with regard to zircon geochronology. Namely that the zircon U-Th-Pb geochronometer can be metasomatically reset, which is an idea that has long been speculated upon in the literature (Hoskin and Schaltegger, 2003; Hoskin, 2005; Geisler et al., 2007; Soman et al., 2010; Van Lankvelt et al., 2016; Peterman et al., 2016; Aranovich et al., 2017; Chen and Zhou, 2017; Wang et al., 2018; Zi et al., 2022). Natural resetting of this geochronometer via Pb diffusion in zircon under fluid-absent conditions has been demonstrated to be a very slow, almost negligible process even if the zircon experiences relatively high temperatures (> 900 °C) for at least 1 Myr (Möller et al., 2002; see also Cherniak and Watson, 2000). In the experiments from this study, the geochronometer was reset due to alkali-bearing high pH or alkali-fluoride fluids at 900 °C and 1000 MPa over a period of days. Such fluids might explain the zircon alteration textures seen in Figure 1 since each of these examples occur in granitoid rocks rich in alkali-bearing feldspars, which have experienced metasomatism/metamorphism under high-grade conditions. In each of these cases, the CL-bright metasomatized areas tend to be younger by some millions to 10's of millions of years than the CL-dark zircon cores, which the authors generally tend to attribute to metamorphic/metasomatic processes. Similar conclusions were reached by Lewerentz et al. (2019) in experiments (600 – 900 °C; 600 – 1000 MPa) involving the partial alteration of a natural zircon in $CaCl_2$- and $Ca(OH)_2$-bearing fluids to baddeleyite. While the newly formed baddeleyite and altered areas in the zircon contained U, Th, and Y + REE derived from the

zircon, Pb in both the baddeleyite and the altered areas of the zircon was below the detection limit of the SIMS.

The depletion of the Y + HREE in the altered areas of the zircon (Fig. 7) is due in part to the fact that the alkali-bearing fluids used in these experiments contained negligible amounts of REE. This apparently allowed for a fraction of the Y+HREE to be partitioned into the fluid where they presumably complexed with OH^- (ZF-5 and ZF-9) (Haas et al., 1995; Wood et al., 2002; Pourtier et al., 2010; Perry and Gysi, 2018) and/or with F^- (ZF-16 and ZF-40) (Haas et al., 1995; Tropper et al., 2011, 2013; Mair et al., 2017). Depletion or enrichment of REE in zircon is a commonly observed phenomena in granitoid rocks and generally presumed due to metasomatically induced alteration via fluids and/or melts. Examples include zircons with metasomatically altered areas depleted in REE from fluid-induced charnockite patches in granitoid rocks from Kottavattom, Trivandrum Block, southern India (Taylor et al., 2014); metasomatically altered areas depleted in REE in metamorphosed zircons from the leucocratic portion of a migmatite, Ticino, Switzerland (Vonlanthen et al., 2012); and zircons from high grade metagranitoids, Queensland, Australia where the metasomatically altered areas are depleted in REE (Hoskin and Black, 2000).

5. Summary and implications

In this study it has been demonstrated in a series of experiments that natural zircon with relatively small amounts of radiation damage can be metasomatically altered using alkali- and F-bearing solutions under the high grade P-T conditions commonly found in the lower crust. This involved the incorporation of Th and the removal of U and REE, and the near to total removal of Pb to below LA-ICP-MS and SIMS detection limits in the altered areas, which implies a basic resetting of the U-Th-Pb geochronometer. If this is also the case for zircons in nature, then this would imply that similar textures, as illustrated in Figure 1, could be metasomatically induced and thus could potentially be used to date metasomatic events.

A second major implication from these experiments is that if zircon with low radiation damage can be metasomatically altered this would have important consequences with respect to zircons presumed role as an impregnable container for mineral inclusions. Namely the mineral inclusions contained within the zircon could also be altered, reset as a geochronometer, or even replaced by another mineral. This has important consequences especially with respect to how the mineral inclusions within the Hadean detrital zircons from Jack Hills, Australia have been utilized in an attempt to discern the geochemical and physical conditions on the very early Earth during the Hadean period (4.0 – 4.54 Ga) (Mojzsis et al., 2001; Wilde et al., 2001; Valley et al., 2002, 2014). The fact that these inclusions have apparently experienced varying degrees of alteration has been amply demonstrated by Rasmussen et al. (2011) who, in a study of monazite and xenotime inclusions in the 4.35 to 3.35 Ga Jack Hills detrital zircons, concluded that these inclusions formed as the result of a metamorphic event at either 2.68 or 0.8 Ga and at monazite-xenotime temperatures (Gratz and Heinrich, 1997) of around 420 to 475 °C. The Ti content of the quartz inclusions in these same zircons gave temperatures of 350 to 490 °C using the geothermometer of Thomas et al. (2010). They also noted that most of the mineral inclusions have the same composition and abundances as the minerals in the original metamorphic matrix in which the zircons were found. This is consistent with the idea that these inclusions, which include K-feldspar, albite, muscovite, and biotite, formed during metamorphism due perhaps to the replacement of what could have been originally apatite inclusions, which are one of the more common types of mineral inclusions in zircon and generally not observed in Jack Hills zircons. If this replacement of mineral inclusions did occur, it would probably have occurred via a coupled dissolution-reprecipitation process as outlined by the experiments in this study. These observations are backed by a CO_2 fluid inclusion study of the Jack Hills zircons by Menneken et al. (2017). Here the formation of these CO_2 inclusions appears to be related to a later metamorphic event as opposed to the primary igneous event presumed responsible for the genesis of the zircons.

Mineral inclusion formation in zircon grain interiors via a fluid-aided coupled dissolution-reprecipitation process are not limited to the Jack Hills zircons. For example, Troch et al. (2018) documented the fluid-aided formation, via coupled dissolution-reprecipitation, of U-Th-REE phases as mineral inclusions in trace element-rich zircons from the Island Park-Mount Jackson rhyolite, Yellowstone volcanic field, Wyoming, USA. Similar conclusions have also been reached for ultra-high pressure mineral inclusions, such as coesite and jadeite, in zircon from a jadeite quartzite, Dabie orogen, central China (Gao et al., 2015). While the zircons here are presumed to have a detrital, igneous mid-crustal origin, the inclusions could only have formed during a fluid-rich event, perhaps as a result of coupled dissolution-reprecipitation, under the ultra-high pressure metamorphic conditions present during the continental subduction conditions experienced by the jadeite quartzite during the Dabie orogeny.

Similar conclusions have been reached for entirely different mineral systems. For example, Krause et al. (2013) documented metasomatically altered apatite inclusions in clinopyroxene from a nepheline-bearing clinopyroxenite located in the Uralian-Alaskan-type complexes of Kytlym and Nizhny Tagil, Ural Mountains, Russian Federation. Here the clinopyroxene experienced partial metasomatic alteration via coupled dissolution-reprecipitation by a $CaCl_2$-enriched saline fluid, which also altered the apatite inclusions in these areas from fluor-chlorapatite to chlor-fluorapatite giving them a composition similar to the apatites in the surrounding mineral matrix. In those areas of the clinopyroxene not metasomatically altered, the apatites retained their original fluor-chlorapatite composition. In another example, where apatite is the host mineral, the formation of magnetite and quartz inclusions in metasomatically altered areas of fluorapatite from the Pea Ridge iron oxide-apatite ore body is attributed to fluid-aided mass transfer of Fe and Si into the fluorapatite from magnetite and quartz in the surrounding mineral matrix, again during a process of coupled dissolution-reprecipitation (Harlov et al., 2016).

In all of these cases, the key point here is that the chemistry of a fluid encountered by zircon, or any other mineral, will dictate whether or not the mineral will experience alteration, and

whether this alteration occurs by simple partial dissolution, overgrowth, or metasomatic alteration, either partial or total, via a coupled dissolution-reprecipitation process. This last process can also result in the total replacement of one mineral phase by another mineral phase as proposed for the inclusions in the zircon, clinopyroxene, or fluorapatite as discussed above. The pressure and temperature under which such a process will or could occur is of less importance since nature has time on its side as opposed to the very finite lifetime of laboratory experiments (see discussion in Harlov et al., 2002, 2003, 2005).

The basic conclusion here is that if the typical sort of zircon commonly found in crustal rocks, with radiation damage ranging from light to metamict, encounters a chemically reactive fluid, such as the alkali-bearing and F-bearing fluids used in these experiments, it could be partially to totally altered chemically with respect to it trace elements including U, Th, Pb, and the Y+REE. This could result in the U-Th-Pb geochronometer in the altered areas being reset if all the Pb is removed thus allowing for the metasomatic event responsible to be dated. Just as importantly any inclusions in the altered areas of the zircon could also experience potential chemical alteration, depending on their reactivity to the fluid, with respect to both major and trace element composition, or be replaced by other minerals more in equilibrium with both the infiltrating fluid and the mineral assemblage surrounding the zircon.

Declaration of Competing Interest

The authors declare that they have no known competing financial interests or personal relationships that could have appeared to influence the work reported in this paper.

Acknowledgements

Richard Wirth and Anja Schreiber are thanked for their assistance with the focused ion beam sampling and the transmission electron microscopy. Dieter Rhede is thanked for helping to acquire the zircon EPMA data. Special thanks to Prof. Kazuyuki Shiraishi for making available the

analytical facilities of the National Institute of Polar Research available to Daniel Dunkley and Daniel Harlov. Daniel Harlov was supported by an Invitational Fellowship for Research in Japan from the Japan Society for the Promotion of Science (or JSPS Invitational Fellowships for Research in Japan). Special thanks to the Polish Academy of Sciences (Polska Akademia Nauk, PAN) and the Foundation for Polish Science (Fundacja na rzecz Nauki Polskiej, FNP) for supporting the LA-ICP-MS analytical facilities at the Krakow Research Centre (Robert Anczkiewicz) and making them available to Daniel Harlov. Comments by Rongquing Zhang and two anonymous reviewers helped to improve the manuscript.

Appendix A. Supplementary Material

The supplementary materials for this manuscript include four supplementary tables (Tables S1, S2, S3, and S4) and one supplementary figure (Figure S1). Table S1 contains all EPMA data acquired from these zircon metasomatism experiments. Tables S2, S3, and S4 contain all the raw LA-ICP-MS and SHRIMP data utilized to assemble Tables 2 and 3 and the REE chondrite-normalized plots in Figure 7 and Figure S1. In Figure S1, the chondrite normalized REE data from the SHRIMP analyses (Table S3) and the LA-ICP-MS analyses (Table S4) are plotted for comparison. Supplementary materials attached to this article can be found online at ……

~~Supplementary Table 1: Electron probe microanalytical data from experimentally metasomatised zircons~~

~~Supplementary Table 2: Zircon U-Th-Pb SHRIMP analyses~~

~~Supplementary Table 3: SHRIMP REE analyses of experimentally metasomatised zircons~~

~~Supplementary Table 4: GLITTER4.4.2: Laser Th, U, Pb, and REE Ablation Analysis Results~~

~~Supplementary Figure 1: Chondrite normalized plots of SHRIMP and LA-ICP-MS zircon data~~

Formatted: Font: Bold

Formatted: Font color: Red

Formatted: Font color: Red

Formatted: Font color: Custom Color(RGB(4,50,255))

Formatted: Font color: Red

Formatted: Font color: Red

Formatted: Font color: Red

Formatted: Font color: Red

Formatted: Font color: Red

Formatted: Font color: Custom Color(RGB(4,50,255))

Formatted: Font color: Custom Color(RGB(4,50,255))

Formatted: Font color: Red

Formatted: Font color: Red

References

Altree-Williams, A., Pring, A., Ngothai, Y., Brügger, J., 2015. Textural and compositional complexities resulting from coupled dissolution–reprecipitation reactions in geomaterials. Earth Sci. Rev. 150, 628–651.

Aranovich, L.Y., Bortnikov, N.S., Zinger, T.F., Borisovskiy, S.E., Matrenichev, V.A., Pertsev, A.N., Sharkov, E.V., Skolotnev, S.G., 2017. Morphology and impurity elements of zircon in the oceanic lithosphere at the mid-Atlantic ridge axial zone (6°–13° N): evidence of specifics of magmatic crystallization and postmagmatic transformations. Petrology 25, 335–361.

Ayers, J.C., Zhang, L., Luo, Y., Peters, T.J., 2012. Zircon solubility in alkaline aqueous fluids at upper crustal conditions. Geochim. Cosmochim. Acta 96, 18–28.

Ayers, J.C., Peters, T.J., 2018. Zircon/fluid trace element partition coefficients measured by recrystallization of Mud Tank zircon at 1.5 GPa and 800–1000 °C. Geochim. Cosmochim. Acta 223, 60–74.

Baker, D.R., Conte, A.M., Freda, C., Ottolini, L., 2002. The effect of halogens on Zr diffusion and zircon dissolution in hydrous metaluminous granitic melts. Contrib. Mineral. Petrol. 142, 666–678.

Bernini, D., Audètat, A., Dolejs, D., Keppler, H., 2013. Zircon solubility in aqueous fluids at high temperatures and pressures. Geochim. Cosmochim. Acta 119, 178–187.

Black, L.P., Kamo, S.L., Allen, C.M., Davis, D.W., Aleinikoff, J.N., Valley, J.W., Mundilf, R., Campbell, I.H., Korscha, I.J., Williams, I.S., Foudoulis, C., 2004. Improved $^{206}Pb/^{238}U$ microprobe geochronology by the monitoring of a trace-element-related matrix effect; SHRIMP, ID–TIMS, ELA–ICP–MS and oxygen isotope documentation for a series of zircon standards. Chem. Geol. 205, 115–140.

Borisov, A., Aranovich, L., 2019. Zircon solubility in silicate melts: New experiments and probability of zircon crystallization in deeply evolved basic melts. Chem. Geol. 510, 103–112.

Bottari, E., Ciavatta, L., 1965. On the complex formation between lead(II) and fluoride ions. J. Inorg. Nucl. Chem. 27, 133–141.

Chatterjee, N., Crowley, J.L., Mukherjee, A., Das, S., 2008. Geochronology of the 983-Ma Chilka lake anorthosite, Eastern Ghats Belt, India: implications for Pre-Gondwana tectonics. J. Geol. 116, 105–118.

Chen, W.T., Zhou, M.-F., 2017. Hydrothermal alteration of magmatic zircon related to NaCl-rich

Formatted: English (United States)

brines: diffusion-reaction and dissolution-reprecipitation processes. Am. J. Sci. 317, 177–215.

Cherniak, D.J., Hanchar, J.M., Watson, E.B., 1997a. Diffusion of tetravalent cations in zircon. Contrib. Mineral. Petrol. 127, 383–390.

Cherniak, D.J., Hanchar, J.M., Watson, E.B., 1997b. Rare earth diffusion in zircon. Chem. Geol. 134, 289–301.

Cherniak, D.J., Watson, E.B., 2000. Pb diffusion in zircon. Chem. Geol. 172, 5–24.

Ende, M., Chanmuang N.C., Reiners, P.W., Zamyatin, D.A., Gain, S.E.M., Wirth, R., Nasdala, L., 2021. Dry annealing of radiation-damaged zircon: single-crystal X-ray and Raman spectroscopy study. Lithos 406–407, 106523.

Ferry, J.M., Watson, E.B., 2007. New thermodynamic models and revised calibrations for the Ti-in-zircon and Zr-in rutile thermometers. Contrib. Mineral. Petrol. 154, 429–437.

Finch, R.J., Hanchar, J.M., Hoskin, P.W.O., Burns, P.C., 2001. Rare-earth elements in synthetic zircon: Part 2. a single-crystal X-ray study of xenotime substitution. Am. Mineral. 86, 681–689.

Finch, R.J., Hanchar, J.M., 2003. Structure and chemistry of zircon and zircon-group minerals. Rev. Mineral. Geochem. 53, 1–25.

Fougerouse, D., Reddy, S.M., Saxey, D.W., Erickson, T.M., Kirkland, C.L., Rickard, W.D.A., Seydoux-Guillaume, A.-M., Clark, C., Buick, I.S., 2018. Nanoscale distribution of Pb in monazite revealed by atom probe microscopy. Chem. Geol. 479, 251–258.

Gao, X.-Y., Zheng, Y.-F., Chen, Y.-X., Tang H.-L., Li, W.-C., 2015. Zircon geochemistry records the action of metamorphic fluid on the formation of ultra-high-pressure jadeite quartzite in the Dabie orogen. Chem. Geol. 419, 158–175.

Gauthiez-Putallaz, L., Rubatto, D., Hermann, J., 2016. Dating prograde fluid pulses during subduction by in situ U-Pb and oxygen isotope analysis. Contrib. Mineral. Petrol. 171, 15.

Geisler, T., Ulonska, M., Schleicher, H., Pidgeon, R.T., van Bronswijk, W., 2001a. Leaching and differential recrystallization of metamict zircon under experimental hydrothermal conditions. Contrib. Mineral. Petrol. 141, 53–65.

Geisler, T., Pidgeon, R.T., van Bronswijk, W., Pleysier, R., 2001b. Kinetics of thermal recovery and recrystallization of partially metamict zircon: a Raman spectroscopic study. Eur. J. Mineral. 13, 1163–1176.

Geisler, T., Pidgeon, R.T., van Bronswijk, W., Kurtz, R., 2002. Transport of uranium, thorium, and lead in metamict zircon under low-temperature hydrothermal conditions. Chem. Geol. 191, 141–154.

Formatted: English (United States)

Geisler, T., Pidgeon, R.T., Kurtz, R., van Bronswijk, W., Schleicher, H., 2003. Experimental hydrothermal alteration of partially metamict zircon. Am. Mineral. 88, 1496–1513.

Geisler, T., Seydoux-Guillaume, A.-M., Wiedenbeck, M., Wirth, R., Berndt, J., Zhang, M., Mihailova, B., Putnis, A., Salje, E.K.H., Schlüter, J., 2004. Periodic precipitation pattern formation in hydrothermally treated metamict zircon. Am. Mineral. 89, 1341–1347.

Geisler, T., Schaltegger, U., Tomaschek, F., 2007. Re-equilibration of zircon in aqueous fluids and melts. Elements 3, 43-50.

Ginster, U., Reiners, P.W., Nasdala, L., Chanmuang N., C., 2019. Annealing kinetics of radiation damage in zircon. Geochim. Cosmochim. Acta 249, 225–246.

Gratz, R., Heinrich, W., 1997. Monazite-xenotime thermobarometry: Experimental calibration of the miscibility gap in the binary system $CePO_4$-YPO_4. Am. Mineral. 82, 772–780.

Griffin, W., Powell, W., Pearson, N., O'Reilly, S., 2008. GLITTER: Data reduction software for laser ablation ICP-MS: Mineralogical Association of Canada Short Course, v. 40.

Haas, J.R., Shock, E.L., Sassani, D.C., 1995. Rare earth elements in hydrothermal systems: estimates of standard partial molal thermodynamic properties of aqueous complexes of the rare earth elements at high pressures and temperatures. Geochim. Cosmochim. Acta 59, 4329–4350.

Harley, S.L., Kelly, N.M., 2007. Zircon tiny but timely. Elements 3, 13–18.

Harlov, D.E., Förster, H.-J., Nijland, T.G., 2002. Fluid-induced nucleation of (Y + REE)-phosphate minerals within apatite: nature and experiment. Part I. chlorapatite. Am. Mineral. 87, 245–261.

Harlov, D.E., Förster, H.-J., 2003. Fluid-induced nucleation of REE phosphate minerals within apatite: nature and experiment. Part II. fluorapatite. Am. Mineral. 88, 1209–1229.

Harlov, D.E., Wirth, R., Förster, H.-J., 2005. An experimental study of dissolution-reprecipitation in fluorapatite: fluid infiltration and the formation of monazite. Contrib. Mineral. Petrol. 150, 268–286.

Harlov, D.E., Wirth, R., Hetherington, C.J., 2007. The relative stability of monazite and huttonite at 300–900 °C and 200–1000 MPa: metasomatism and the propagation of metastable mineral phases. Am. Mineral. 92, 1652–1664.

Harlov, D.E., Wirth, R., Hetherington, C.J., 2011. Fluid-mediated partial alteration in monazite: the role of coupled dissolution–reprecipitation in element redistribution and mass transfer. Contrib. Mineral. Petrol. 162, 329–348.

Harlov, D.E., Wirth, R., 2012. Experimental incorporation of Th into xenotime at middle to lower crustal P-T utilizing alkali-bearing fluids. Am. Mineral. 97, 641–652.

Harlov, D.E., Meighan, C.J., Kerr, I.D., Samson, I.M., 2016. Mineralogy, chemistry, and fluid-aided evolution of the Pea Ridge Fe oxide-(Y + REE) deposit, southeast Missouri, USA. Econ. Geol. 111, 1963–1984.

Harlov, D.E., Dunkley, D.J., Hansen, E.C., Ishwar-Kumar, C., Samuel, V., Hokada, T., 2022. Zircon as a recorder of trace element changes during high grade metamorphism of Neoarchean lower crust, Shevaroy Block, Eastern Dharwar Craton, India. J. Petrol. 63, egac036.

Härtel, B., Jonckheere, R., Ratschbacher, L., 2022. Multi-band Raman analysis of radiation damage in zircon for thermochronology: partial annealing and mixed signals. Geochem. Geophys. Geosys. 23, e2021GC010182.

Herrmann, M., Söderlund, U., Scherstén, A., Næraa, T., Holm-Alwmark, S., Alwmark, C., 2021. The effect of low‐temperature annealing on discordance of U–Pb zircon ages. Sci. Rept. 11, 7079.

Hoskin, P.W.O., 2005. Trace-element composition of hydrothermal zircon and the alteration of Hadean zircon from the Jack Hills, Australia. Geochim. Cosmochim. Acta 69, 637–648.

Hoskin, P.W.O., Black, L.P., 2000. Metamorphic zircon formation by solid-state recrystallization of protolith igneous zircon. J. Metamorph. Geol. 18, 423–439.

Hoskin, P.W.O., Schaltegger, U., 2003. The composition of zircon and igneous and metamorphic petrogenesis. Rev. Mineral. Geochem. 53, 27–62.

Iizuka, T., Hirata, T., 2004. Simultaneous determinations of U-Pb age and REE abundances for zircons using ArF excimer laser ablation-ICPMS. Geochem. J. 38, 229–241.

Jarosewich, E., Nelen, J.A., Norberg, J.A., 1980. Reference samples for electron microprobe analysis. Geostand. Newslett. 4, 43–47.

Jarosewich, E., Boatner, L.A., 1991. Rare-earth element reference samples for electron microprobe analysis. Geostand. Newslett. 15, 397–399.

Jochum, K.P., Weis, U., Stoll, B., Kuzmin, D., Yang, Q., Raczek, I., Jacob, D.E., Stracke, A., Birbaum, K., Frick, D.A., Günther, D., Enzweiler, J., 2011. Determination of reference values for NIST SRM 610-617 glasses following ISO guidelines. Geostand. Geoanal. Res. 35, 397–429.

Johannes, W., Bell, P.M., Mao, H.K., Boettcher, A.L., Chipman, D.W., Hays, J.F., et al., 1971. An interlaboratory comparison of piston-cylinder pressure calibration using the albite-breakdown reaction. Contrib. Mineral. Petrol. 32, 24–38.

Johannes, W., 1973. A simplified piston-cylinder apparatus of high precision. N. Jahrb. Mineral. Monat. 7, 331–351.

Kogawa, M., Watson, E.B., Ewing, R.C., Utsunomiya, S., 2012. Lead in zircon at the atomic scale. Am. Mineral. 97, 1094–1102.

Krause, J., Harlov, D.E., Pushkarev, E.V., Brügmann, G.E., 2013. Apatite and clinopyroxene as tracers for metasomatic processes in nepheline clinopyroxenites of Uralian-Alaskan-type complexes in the Ural Mountains, Russian Federation. Geochim. Cosmochim. Acta 121, 503–521.

Lenting, C., Geisler, T., Gerdes, A., Kooijman, E., Scherer, E.E., Zeh, A., 2010. The behaviour of the Hf isotope system in radiation-damaged zircon during experimental hydrothermal alteration. Am. Mineral. 95, 1343–1348.

Lewerentz, A., Harlov, D.E., Schersten, A., Whitehouse, M.J., 2019. Baddeleyite formation in zircon by Ca‐bearing fluids in silica‐saturated systems in nature and experiment: resetting of the U-Pb geochronometer. Contrib. Mineral. Petrol. 174, 64.

Ludwig, K.R., 2001. SQUID: A User's Manual: Berkeley Geochronology Center, Special Publication 2, 22 pp.

Ludwig, K.R., 2003. User's manual for Isoplot 3.00: A geochronological toolkit for Microsoft Excel: Berkeley Geochronology Center, Special Publication 4, 71 pp.

Lyon, I.C., Kusiak, M.A., Wirth, R., Whitehouse, M.J., Dunkley, D.J., Wilde, S.A., Schaumlöffel, D., Malherbe, J., Moore, K.L., 2019. Pb nanospheres in ancient zircon yield model ages for zircon formation and Pb mobilization. Sci. Rept. 9, 13702.

Mair, P., Tropper, P., Harlov, D.E., Manning, C.E., 2017. The solubility of $CePO_4$ monazite and YPO_4 xenotime in KCl-H_2O fluids at 800 °C and 1.0 GPa: implications for REE transport in high-grade crustal fluids. Am. Mineral. 102, 2457–2466.

McDonough, W.F., Sun S., 1995. The composition of the Earth. Chem. Geol. 120, 223–253.

Menneken, M., Geisler, T., Nemchin, A.A., Whitehouse, M.J., Wilde, S.A., Gasharova, B., Pidgeon, R.T., 2017. CO_2 fluid inclusions in Jack Hills zircons. Contrib. Mineral. Petrol. 172, 66.

Mezger, K., Krogstad, E.J., 1997. Interpretation of discordant U-Pb zircon ages: an evaluation. J. Metamorph. Geol. 15, 127–140.

Mojzsis, S.J., Harrison, T.M., Pidgeon, R.T., 2001. Oxygen-isotope evidence from ancient zircons for liquid water at the Earth's surface 4,300 Myr ago. Nature 409, 178–181.

Möller, A., O'Brien, P.J., Kennedy, A., Kröner, A., 2002. Polyphase zircon in ultrahigh-temperature granulites (Rogaland, SW Norway): constraints for Pb diffusion in zircon. J. Metamorph. Geol. 20, 727–740.

Montario, M.J., Garver, J.I., Marsellos, A., 2008. Annealing of radiation damage in a Grenville

zircon, from the eastern Adirondacks, NY State. In Garver, J.I., and Montario, M.J. (eds.), Proceedings from the 11th International Conference on thermochronometry, Anchorage Alaska, Sept. 2008.

Morales, I., Molina, J.F., Cambeses, A., Montero, P., Bea F., 2022. Experimental annealing of zircon: influence of inclusions on stability, intracrystalline melt migration, common lead leaching, and permeability to fluids. ACS Earth Space Chem. 6, 288–307.

Nasdala, L., Wenzel, M., Vavra, G., Irmer, G., Wenzel, T., Kober, B., 2001. Metamictisation of natural zircon: accumulation versus thermal annealing of radioactivity-induced damage. Contrib. Mineral. Petrol. 141, 125–144.

Nasdala, L., Lengauer, C.L., Hanchar, J.M., Kronz, A., Wirth, R., Blanc, P., Kennedy, A.K., Seydoux-Guillaume, 2002. Annealing radiation damage and the recovery of cathodoluminescence. Chem. Geol. 191, 121–140.

Nasdala, L., Hanchar, J.M., Kronz, A., Whitehouse, M.J., 2005. Long term stability of alpha particle damage in natural zircon. Chem. Geol. 220, 83–103.

Newton, R.C., Manning, C.E., Hanchar, J.M., Colasanti, C.V., 2010. Free energy of formation of zircon based on solubility measurements at high temperature and pressure. Am. Mineral. 95, 52–58.

Park, C., Song, Y., Chung, D., Kang, I.-M., Khulganakhuu, C., Yi, K., 2016. Recrystallization and hydrothermal growth of high U–Th zircon in the Weondong deposit, Korea: record of post-magmatic alteration. Lithos 260, 268–285.

Pedersen, R.B., Dunning, G.R., Robins, B., 1989. U-Pb ages of nepheline syenite pegmatites from the Seiland Magmatic Province, N. Norway. In Gayer, R.A., ed. The Caledonide Geology of Scandinavia. London, Graham and Trotman, pp. 3–9.

Perera, W.N., Hefter, G., Sipos, P.M., 2001. An investigation of the lead(II)-hydroxide system. Inorg. Chem. 40, 3974–3978.

Perry, E.P., Gysi, A.P., 2018. Rare earth elements in mineral deposits: speciation in hydrothermal fluids and partitioning in calcite. Geofluids 2018, 5382480.

Peterman, E.M., Snoeyenbos, D.R., Jercinovic, M.J., Kylander-Clark, A., 2016. Dissolution-reprecipitation metasomatism and growth of zircon within phosphatic garnet in metapelites from western Massachusetts. Am. Mineral. 101, 1792–1806.

Pidgeon, R.T., O'Neil, J.R., Silver, L.T., 1966. Uranium and lead isotopic stability in a metamict zircon under experimental hydrothermal conditions. Science 154, 1538–1540.

Pourtier, E., Devidal, J.-L., Gibert, F., 2010. Solubility measurements of synthetic neodymium

monazite as a function of temperature at 2 kbars, and aqueous neodymium speciation in equilibrium with monazite. Geochim. Cosmochim. Acta 74, 1872–1891.

Putnis, A., 2002. Mineral replacement reactions: from macroscopic observations to microscopic mechanisms. Mineral. Mag. 66, 689–708.

Putnis, A., 2009. Mineral replacement reactions. Rev. Mineral. Geochem. 70, 87–124.

Putnis, A., Putnis, C., 2007. The mechanism of re-equilibration of solids in the presence of a fluid phase. J. Solid State Chem. 180, 1783–1786.

Putnis, A., Austrheim, H., 2010. Fluid-induced processes: metasomatism and metamorphism. Geofluids 10, 254–269.

Putnis, A., Austrheim, H., 2013. Mechanisms of metasomatism and metamorphism on the local mineral scale: the role of dissolution-reprecipitation during mineral re-equilibration. In D.E. Harlov and H. Austrheim, Metasomatism and the Chemical Transformation of Rock, Lecture Notes in Earth System Sciences, Springer-Verlag Berlin Heidelberg, pp. 141–170.

Putnis, C.V., Tsukamoto, K., Nishimura, Y., 2005. Direct observations of pseudomorphism: compositional and textural evolution at a fluid solid interface. Am. Mineral. 90, 1909–1912.

Rasmussen, B., Fletcher, I.R., Muhling, J.R., Gregory, C.J., Wilde, S.A., 2011. Metamorphic replacement of mineral inclusions in detrital zircon from Jack Hills, Australia: implications for the Hadean Earth. Geology 39, 1143–1146.

Rizvanova, N.G., Levchenkov, A., Belous, A.E., Bezmen, N.I., Maslenikov, A.V., Komarov, A.N., Makeev, A.F., Levskiy, L.K., 2000. Zircon reaction and stability of the U-Pb isotope system during interaction with carbonate fluid: experimental hydrothermal study. Contrib. Mineral. Petrol. 139, 101–114.

Rizvanova, N.G., Gaidamako, I.M., Levchenkov, O.A., Bezmen, N.I., Makeev, A.F., Levsky, L.K., 2007. Interaction of metamict zircon with fluids of various composition. Geochem. Internat. 45, 465–477.

Schmidt, C., Rickers, K., Wirth, R., Nasdala, L., Hanchar, J.M., 2006. Low-temperature Zr mobility: an in situ synchrotron-radiation XRF study of the effect of radiation damage in zircon on the element release in H_2O + HCl ± SiO_2 fluids. Am. Mineral. 91, 1211–1215.

Schmidt, C., Steele-MacInnis, M., Watenphul, A., Wilke, M., 2013. Calibration of zircon as a Raman spectroscopic pressure sensor to high temperatures and application to water-silicate melt systems. Am. Mineral. 98, 643–650.

Seydoux-Guillaume, A.-M., Bingen, B., Paquette, J.-L., Bosse, V., 2015. Nanoscale evidence for uranium mobility in zircon and the discordance of U–Pb chronometers. Earth Planet. Sci. Lett. 409, 43–48.

Shannon, R.D., 1976. Revised effective ionic radii and systematic studies of interatomic distances in halides and chalcedonides. Acta Crystal. A32, 751–767.

Soman, A., Geisler, T., Tomaschek, F., Grange, M., Berndt, J., 2010. Alteration of crystalline zircon solid solutions: a case study on zircon from an alkaline pegmatite from Zomba–Malosa, Malawi. Contrib. Mineral. Petrol. 160, 909–930.

Speer, J.A., Cooper, B.J., 1982. Crystal structure of synthetic hafnon, $HfSiO_4$, comparison with zircon and the actinide orthosilicates. Am. Mineral. 67, 804–808.

Stacey, J.C., Kramers, J., 1975. Approximation of terrestrial lead isotope evolution by a two-stage model. Earth Planet. Sci. Lett. 26, 207–221.

Tailby, N.D., Walker, A.M., Berry, A.J., Hermann, J., Evans, K.A., Mavrogenes, J.A., O'Neill, H.St.C., Rodina, I.S., Soldatov, A.V., Rubatto, D., Sutton, S.R., 2011. Ti site occupancy in zircon. Geochim. Cosmochim. Acta 75, 905–921.

Taylor, R.J.M., Clark, C., Fitzsimons, I.C.W., Santosh, M., Hand, M., Evans, N., McDonald, B., 2014. Post-peak, fluid-mediated modification of granulite facies zircon and monazite in the Trivandrum Block, southern India. Contrib. Mineral. Petrol. 168, 1044.

Thomas, J.B., Watson, E.B., Spear, F.S., Shemella, P.T., Nayak, S.K., Lanzirotti, A., 2010. TitaniQ under pressure: the effect of pressure and temperature on the solubility of Ti in quartz. Contrib. Mineral. Petrol. 160, 743–759.

Tomaschek, F., 2004. Zircon re-equilibration by dissolution-reprecipitation: reaction textures from flux-grown solid solutions. Berichte der Deutschen Mineralogischen Geschellschaft Beihefte zum Eur. J. Mineral. 16, 147.

Tomaschek, F., 2010. Praktische Aspekte der Mischkristallphase Zirkon: Reequilibrierungsprozess, Zirkon-Xenotim Mischungslücke, geochronologische Anwendungen in einem polymetamorphen Kristallinkomplex (Syros, Kykladen, Griechenland). Ph.D. thesis Mathematisch Naturwissenschaftlichen Fakultät der Westfälischen Wilhelms-Universität Münster, Münster, Germany, 431 pp.

Trail, D., Cherniak, D.J., Watson, E.B., Harrison, T.M., Weiss, B.P., Szumila, I., 2016. Li zoning in zircon as a potential geospeedometer and peak temperature indicator. Contrib. Mineral. Petrol. 171, 25.

Troch, J., Ellis, B.S., Schmitt, A.K., Bouvier, A.-S., Bachmann, O., 2018. The dark side of zircon: textural, age, oxygen isotopic and trace element evidence of fluid saturation in the subvolcanic reservoir of the Island Park-Mount Jackson Rhyolite, Yellowstone (USA). Contrib. Mineral. Petrol. 173, 54.

Tropper, P., Manning, C.E., Harlov, D.E., 2011. Solubility of $CePO_4$ monazite and YPO_4 xenotime

in H_2O and H_2O-NaCl at 800 °C and 1 GPa: implications for REE and Y transport during high-grade metamorphism. Chem. Geol. 282, 58–66.

Tropper, P., Manning, C.E., Harlov, D.E., 2013. Experimental determination of $CePO_4$ and YPO_4 solubilities in H_2O-NaF at 800 °C and 1 GPa: implications for rare earth element transport in high-grade metamorphic fluids. Geofluids 13, 372–380.

Ushakov, S.V., Gong, W., Yagovkina, M.M., Helean, K.B., Lutze, W., Ewing, R.C., 1999. Solid solutions of Ce, U, and Th in zircon. Ceram. Trans. 93, 357–363.

Utsunomiya, S., Palenik, C.S., Valley, J.W., Cavosie, A.J., Wilde, S.A., Ewing, R.C., 2004. Nanoscale occurrence of Pb in an Archean zircon. Geochim. Cosmochim. Acta 68, 4679–4686.

Valley, J.W., Peck, W.H., King, E.M., Wilde, S.A.W., 2002. A cool early Earth. Geology 30, 351–354.

Valley, J.W., Cavosie, A.J., Ushikubo, T., Reinhard, D.A., Lawrence, D.F., Larson, D.J., Clifton, P.H., Kelly, T.F., Wilde, S.A., Moser, D.E., Spicuzza, M.J., 2014. Hadean age for a post-magma-ocean zircon confirmed by atom-probe tomography. Nature Geosci. 7, 219–223.

Valley, J.W., Reinhard, D.A., Cavosie, A.J., Ushikubo, T., Lawrence, D.F., Larson, D.J., Kelly, T.F., Snoeyenbos, D.R., Strickland, A., 2015. Nano- and micro-geochronology in Hadean and Archean zircons by atom-probe tomography and SIMS: new tools for old minerals. Am. Mineral. 100, 1355–1377.

Van Lankvelt, A., Schneider, D.A., Biczok, J., McFarlane, C.R.M., Hattori, K., 2016. Decoding zircon geochronology of igneous and alteration events based on chemical and microstructural features: a study from the Western Superior Province, Can. J. Petrol. 57, 1309–1334.

Vonlanthen, P., Fitz Gerald, J.D., Rubatto, D., Hermann, J., 2012. Recrystallization rims in zircon (Valle d'Arbedo, Switzerland): an integrated cathodoluminescence, LA-ICP-MS, SHRIMP, and TEM study. Am. Mineral. 97, 369–377.

Wang, R., Jeon, H., Evans, N.J., 2018. Archaean hydrothermal fluid modified zircons at Sunrise Dam and Kanowna Belle gold deposits, Western Australia: implications for post-magmatic fluid activity and ore genesis. Am. Mineral. 103, 1891–1905.

Wang, Y., Trail, D., 2022. Experimental partitioning of Li between zircon and different silicate melts: implications for Li contents in the Hadean and modern crust. Contrib. Mineral. Petrol. 177, 15.

Watson, B., Cherniak, D.J., Hanchar, J.M., Harrison, T.M., Wark, D.A., 1997. The incorporation of Pb into zircon. Chem. Geol. 141, 19–31.

Formatted: English (United States)

Watson, E.B., Harrison, T.M., 2005. Zircon thermometer reveals minimum melting conditions on earliest Earth. Science 308, 841–844.

Watson, E.B., Wark, D.A., Thomas, J.B., 2006. Crystallization thermometers for zircon and rutile. Contrib. Mineral. Petrol. 151, 413–433.

Wiedenbeck, M., Hanchar, J.M., Peck, W.H., Sylvester, P., Valley. J., Whitehouse, M., Kronz, A., Morishita, Y., Nasdala, L., Fiebig, J., Franchi, I., Girard, J.-P., Greenwood, R.C., Hinton, R., Kita, N., Mason, P.R.D., Norman, M., Ogasawara, M., Piccoli, P.M., Rhede, D., Satoh, H., Schulz-Dobrick, B., Skår, O., Spicuzza, M.J., Terada, K., Tindle, A., Togashi, S., Vennemann, T., Xie, Q., Zheng, Y.-F., 2004. Further characterisation of the 91500 zircon crystal. Geostand. Geoanal. Res. 28, 9–39.

Wilde, S.A., Valley, J.W., Peck, W.H., Graham, C.M., 2001. Evidence from detrital zircons for the existence of continental crust and oceans on the Earth 4.4 Gyr ago. Nature 409, 175–178.

Wilke, M., Schmidt, C., Dubrail, J., Appel, K., Borchert, M., Kvashina, K., Manning, C.E., 2012. Zircon solubility and zirconium complexation in H_2O + Na_2O + SiO_2 +/- Al_2O_3 fluids at high pressure and temperature. Earth Planet. Sci. Lett. 349-350, 15–25.

Wirth, R., 2004. Focused ion beam (FIB): A novel technology for advanced application of micro- and nano-analysis in geosciences and applied mineralogy. Eur. J. Mineral. 15, 863–875.

Wirth, R., 2009. Focused Ion Beam (FIB) combined with SEM and TEM: advanced analytical tools for studies of chemical composition, microstructure and crystal structure in geomaterials on a nanometre scale. Chem. Geol. 261, 217–229.

Wood, S.A., Palmer, D.A., Wesolowski, D.J., B´en´ezeth, P., 2002. The aqueous geochemistry of the rare earth elements and yttrium. Part XI. the solubility of $Nd(OH)_3$ and hydrolysis of Nd^{3+} from 30 to 290 °C at saturated water vapor pressure with in-situ pHm measurement. In Water-Rock Interactions, Ore Deposits, and Environmental Geochemistry: A Tribute to David A. Crerar, R. Hellmann and S. A. Wood, Eds., vol. 7, 229–256.

Zi, J.W., Rasmussen, B., Muhling, J.R., Fletcher, I.R., 2022. In situ U-Pb and geochemical evidence for ancient Pb-loss during hydrothermal alteration producing apparent young concordant zircon dates in older tuffs. Geochim. Cosmochim. Acta 320, 324–338.

Figures

Figure 1: CL images of zircon from (**a,b**) the Shevaroy Massif (granulite-facies charnockite), Tamil Nadu, southern India (Harlov et al., 2022); (**c**) an anorthsite, Eastern Ghats Belt, India (Chatterjee et al., 2008; their Figure 2B); (**d**) polymetamorphic migmatites, Valle d'Arbedo, Ticino, Switzerland (Vonlanthen et al., 2012); (**e**) high-grade granulite-facies metagranitoids, Queensland, Australia (Hoskin and Black, 2000); and (**f**) a granitic gneiss in the contact aureole of the Rogaland anorthosite-norite intrusive complex, southwest Norway (Möller et al., 2002). Terms sz, oz, and og in Figure 1c stand for sector zoned, oscillatory zoned, and over growth, respectively. In Figure 1d, the circles 5a, 5b, 5c, and 5d indicate areas where TEM foils were cut. In Figure 1e, P stands for protolith zircon; C_1 and C_2 stands for inherited core; OZP stands for oscillatory zircon; and the scale bars are all 50 µm. Under CL imaging for all images, the light areas in the zircon are depleted in Th and U relative to dark areas in the zircon.

Figure 2: (**a**) BSE and (**b**) CL images of a grain fragment of the starting zircon from a nepheline syenite pegmatite, Seiland igneous province, northern Norway.

Figure 3: Sketch of the CaF_2 assembly used in the experiments with the piston cylinder apparatus showing the location of the four Pt capsules separated by biotite sheets.

Figure 4: (**a,c,d**) CL images of a zircon grain fragment reacted in a $Na_2Si_2O_5$ + H_2O solution + ThO_2 + $ThSiO_4$ + SiO_2 at 900 °C and 1000 MPa. Altered areas (light areas in CL) are enriched in Th and depleted in U, Pb, and (Y+REE) (see Tables 2 and 3). Figure 4b is a TEM foil taken from the elongated area located across the reaction front shown in Figure 4a. Note the lack of any reaction texture in the TEM foil nor the indication of a reaction front (the sharp boundary between

light and dark areas in Figure 4b). Dark ovals in the background are from the carbon foil upon which the TEM foil rests.

Figure 5: BSE (**a**) and CL (**b**) images of a zircon grain fragment reacted in a 2N NaOH solution + ThO_2 + $ThSiO_4$ + SiO_2 at 900 °C and 1000 MPa. Altered areas (light areas in CL) are enriched in Th and depleted in U, Pb, and (Y+REE) (see Tables 2 and 3). Figure 5b is a TEM foil taken from the elongated area across the reaction front shown in Figure 5a. Note the lack of any reaction texture in the TEM foil nor the indication of a reaction front (the sharp boundary between light and dark areas in Figure 5b). Dark ovals in the background are from the carbon foil upon which the TEM foil rests.

Figure 6: (**a,c,d,e,f**) CL images of zircon reacted in a NaF + H_2O solution + ThO_2 + $ThSiO_4$ + SiO_2 at 900 °C and 1000 MPa. Altered areas (light areas in CL) are enriched in Th and depleted in U, Pb, and (Y+REE) (see Tables 2 and 3). Figure 6b is a TEM foil taken from the elongated area across the reaction front shown in Figure 6a. Note the lack of any reaction texture in the TEM foil nor the indication of a reaction front (the sharp boundary between light and dark areas in Figure 6b). Dark ovals in the background are from the carbon foil upon which the TEM foil rests. Note also the overgrowth of zircon near the top of Figure 6a (sharp crystallographic faces) and compare this to the lack of crystallographic faces along the bottom of the grain where intergrowth occurs into the zircon body via fluid-aided coupled dissolution-reprecipitation. In Figures 6e and 6f alteration is seen along cracks and possible cleavage planes in the zircon.

Figure 7: Chondrite normalized (McDonough and Sun, 1995) plots of Y + HREE from altered and unaltered areas of zircon in experiments (**a**) ZF-5 ($Na_2Si_2O_5$ + H_2O), (**b**) ZF-9 (2N NaOH), (**c**) ZF-16 (NaF + H_2O), and (**d**) ZF-40 (NaF + H_2O) (see Tables 2 and 3; ~~Supplementary Material~~ Table S4).

Table 1. Experimental results from metasomatic alteration of zircon.

Experiment	P (MPa)	T (°C)	Time (h)	Zrn	Th,Si Mix	NaCl	KCl	NaF	$Na_2Si_2O_5$	H_2O	2N NaOH	2N KOH	Results
ZF-4	1000	900	144	22.54	5.2					6.4			no reaction
ZF-5	1000	900	144	21.03	5.08				10.23	5.6			reaction
ZF-6	1000	900	144	20.43	4.09							6.17	no reaction
ZF-9	1000	900	147	21.79	4.83						5.55		reaction
ZF-12	1000	900	142	19.24	4.97		3.19			2.18			no reaction
ZF-13	1000	900	144	21.85	5.02	2.63				2.18			no reaction
ZF-16	1000	900	132	20.31	4.42			1.12		4.98			strong reaction
ZF-40	1000	900	192	13.06	2.00			2.41		7.27			strong reaction

Solid and fluid in mg

Table 2. Representative SHRIMP analyses of zircon (ppm) experimentally metasomatised at 900 °C and 1000 MPa in a series of alkali-bearing fluids.

	ZF-5				ZF-9[c]		ZF-16			
fluid	$ThO_2 + ThSiO_4 + SiO_2 + Na_2Si_2O_5 + H_2O$				$ThO_2 + ThSiO_4 + SiO_2 + 2N\ NaOH$		$ThO_2 + ThSiO_4 + SiO_2 + NaF + H_2O$			
zircon area	unaltered		altered		unaltered	altered	unaltered		altered	
Element		1s[a]	Mean	1s[b]			Mean	1s[b]	Mean	1s[b]
Y89	240	*1.30*	123	*1.63*			209	*2.19*	24.3	*10.2*
La139	0.01	*0.01*	0.03	*0.01*			0.03	*0.02*	0.03	*0.00*
Ce140	3.23	*0.08*	0.06	*0.03*			2.67	*0.18*	0.05	*0.01*
Pr141	0.01	*0.01*	0.02	*0.00*			0.01	*0.01*	0.02	*0.01*
Nd146	0.15	*0.13*	0.06	*0.09*			0.17	*0.15*	0.10	*0.08*
Sm147	0.33	*0.04*	0.01	*0.02*			0.38	*0.19*	0.02	*0.03*
Eu153	0.57	*0.04*	0.06	*0.02*			0.40	*0.05*	0.02	*0.02*
Gd157	2.19	*0.26*	3.63	*2.09*			2.36	*0.24*	0.02	*0.03*
Tb159	1.21	*0.03*	0.16	*0.04*			1.18	*0.09*	0.08	*0.03*
Dy163	16.8	*0.60*	2.19	*1.51*			15.2	*0.94*	1.53	*0.78*
Ho165	7.09	*0.15*	1.64	*0.72*			6.69	*0.12*	1.18	*0.52*
Er166	37.4	*0.46*	10.1	*6.07*			31.8	*0.15*	7.91	*3.21*
Tm169	8.43	*0.20*	3.49	*2.29*			7.77	*0.16*	2.53	*0.63*
Yb172	88.1	*4.48*	40.1	*25.5*			78.1	*1.18*	28.1	*8.36*
Lu175	17.2	*1.24*	7.87	*7.40*			16.8	*0.93*	7.29	*1.65*
Hf178	4731	*152*	4598	*58.3*			4360	*116*	4715	*207*
Rad 206Pb	4.56		bd		5.06	bd	3.68		bd	
Th	51.1		1197		50.6	1070	37.4		457	
U	61.1		5.5		66.8	4.22	47.8		0.33	

a - instrumental error; b - mean error; c - REE not measured; bd - below detection limit; Rad - radiogenic.

Table 3. LA-ICPMS analysis of zircon (ppm) experimentally metasomatised at 900 °C and 1000 MPa in a series of alkali-bearing fluids.

	ZF-5				ZF-9			ZF-16				ZF-40			
fluid	ThO_2 + $ThSiO_4$ + SiO_2 + $Na_2Si_2O_5$ + + H_2O				ThO_2 + $ThSiO_4$ + SiO_2 + 2N + NaOH			ThO_2 + $ThSiO_4$ + SiO_2 + NaF + H_2O				ThO_2 + $ThSiO_4$ + SiO_2 + NaF + + H_2O			
zircon area	unaltered		altered		unaltered		altered	unaltered		altered		unaltered		altered	
#pts	2		2		7		1	4		5		16		18	
Element	Mean	1s	Mean	1s	Mean	1s		Mean	1s	Mean	1s	Mean	1s	Mean	1s
P31*	72.0	*4.2*	89.2	*24.5*	90.8	*45.2*	19.7	38.7	*14.2*	35.8	*9.13*	65.4	*19.4*	52.1	*16.7*
Ti47	2350	*40.3*	2214	*96.6*	2254	*79.3*	2152	2340	*28.3*	2343	*60.1*	2182	*31.5*	2188	*27.3*
Y89	243	*0.50*	116	*3.40*	213	*22.9*	90.5	209	*3.64*	44.8	*17.9*	250	*27.5*	67.9	*17.5*
La139	0.00	*0.00*	0.01	*0.01*	0.01	*0.02*	0.00	0.00	*0.00*	0.00		0.00	*0.00*	0.00	*0.00*
Ce140	3.68	*0.08*	0.02	*0.03*	3.11	*0.26*	0.26	3.16	*0.17*	0.03	*0.06*	3.39	*0.40*	6.97	*1.03*
Pr141	0.02	*0.02*	0.00	*0.01*	0.01	*0.02*	0.00	0.01	*0.01*	0.00	*0.01*	0.01	*0.02*	0.00	*0.00*
Nd146	0.11	*0.16*	0.06	*0.09*	0.16	*0.12*	0.00	0.15	*0.04*	0.01	*0.02*	0.24	*0.18*	0.02	*0.02*
Sm147	0.56	*0.00*	0.03	*0.04*	0.34	*0.23*	0.00	0.43	*0.10*	0.02	*0.02*	0.63	*0.28*	0.05	*0.04*
Eu153	0.59	*0.02*	0.00	*0.00*	0.43	*0.10*	0.00	0.49	*0.06*	0.03	*0.04*	0.59	*0.19*	0.03	*0.02*
Gd157	3.25	*0.16*	4.95	*1.58*	3.27	*0.66*	0.49	3.14	*0.09*	0.15	*0.12*	3.83	*0.87*	0.73	*0.20*
Tb159	1.58	*0.16*	0.24	*0.05*	1.29	*0.18*	0.39	1.32	*0.04*	0.19	*0.06*	1.60	*0.33*	0.55	*0.14*
Dy163	20.4	*0.72*	3.50	*0.66*	18.2	*2.29*	3.92	18.0	*0.33*	3.67	*1.56*	21.9	*2.93*	8.84	*2.29*
Ho165	8.37	*0.35*	2.10	*0.61*	7.45	*1.10*	3.02	7.46	*0.24*	2.39	*1.05*	8.81	*1.13*	4.23	*1.05*
Er166	46.5	*1.66*	16.9	*2.52*	38.9	*4.85*	18.5	38.3	*1.13*	17.0	*7.22*	45.9	*5.02*	25.4	*6.12*
Tm169	10.2	*0.33*	5.51	*0.79*	9.54	*1.21*	6.12	9.18	*0.26*	5.61	*2.41*	10.6	*0.90*	6.52	*1.61*
Yb172	106	*1.59*	65.6	*4.68*	93.3	*11.1*	54.0	93.5	*3.41*	62.0	*24.0*	108	*8.79*	70.6	*17.1*
Lu175	21.0	*0.50*	15.7	*0.40*	18.8	*2.08*	18.7	17.8	*0.56*	14.7	*5.43*	20.9	*1.61*	14.9	*3.45*
Hf178	6242	*203*	5770	*169*	6160	*567*	5483	5772	*58.9*	5996	*495*	5622	*288*	5752	*87.7*
Pb208	2.88	*0.07*	0.23	*0.32*	2.39	*0.33*	0.33	1.93	*0.17*	0.01	*0.02*	2.48	*0.64*	0.01	*0.01*
Th232	49.7	*2.57*	775	*5.46*	45.5	*6.41*	693	42.5	*2.39*	23124	*48201*	47.6	*11.4*	601	*142*
U238	62.4	*1.85*	3.13	*0.49*	53.7	*5.03*	6.76	52.3	*2.16*	5.84	*1.99*	56.1	*9.28*	0.00	*0.01*

* - approximate values for P, i.e. less than the value stated.

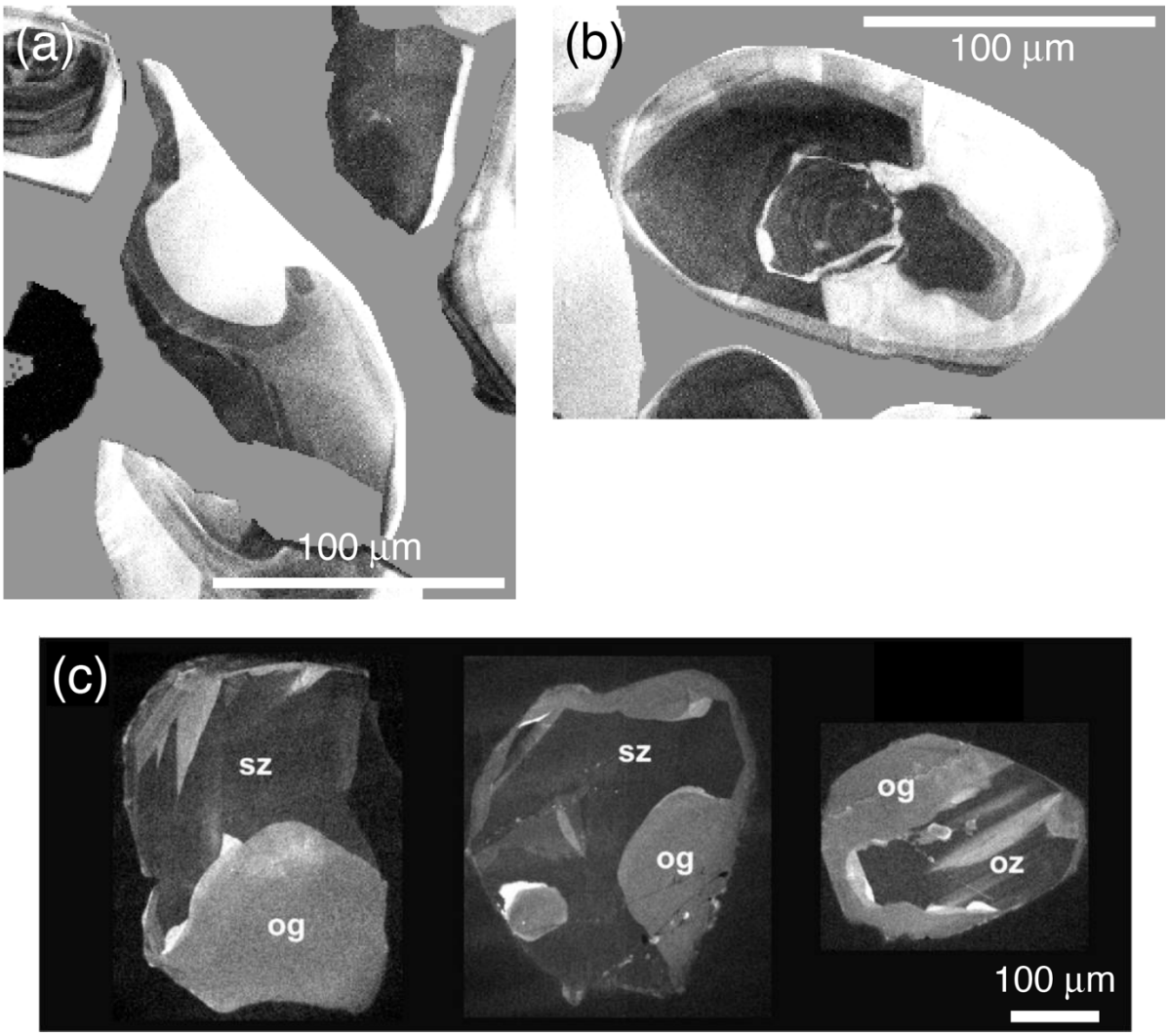

(d)

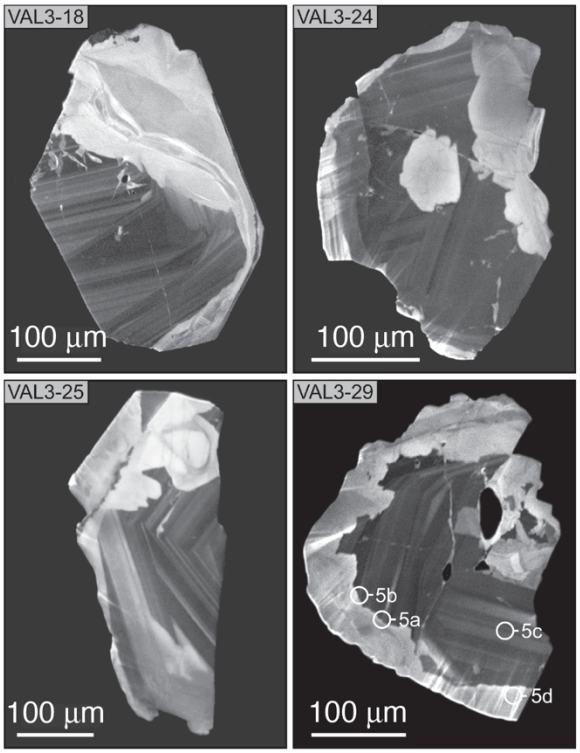
VAL3-18
100 µm
VAL3-24
100 µm
VAL3-25
100 µm
VAL3-29
5b
5a
5c
5d
100 µm

(e)

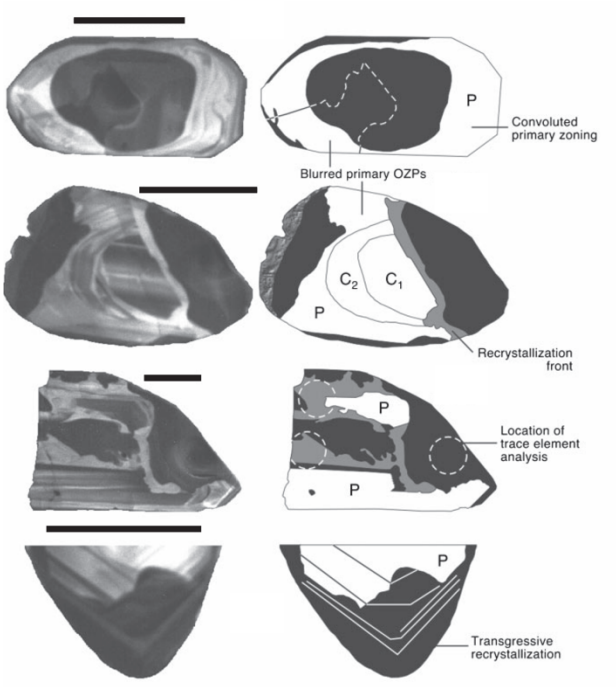
P
Convoluted primary zoning
Blurred primary OZPs
C2
C1
P
Recrystallization front
P
Location of trace element analysis
P
P
Transgressive recrystallization

(f)

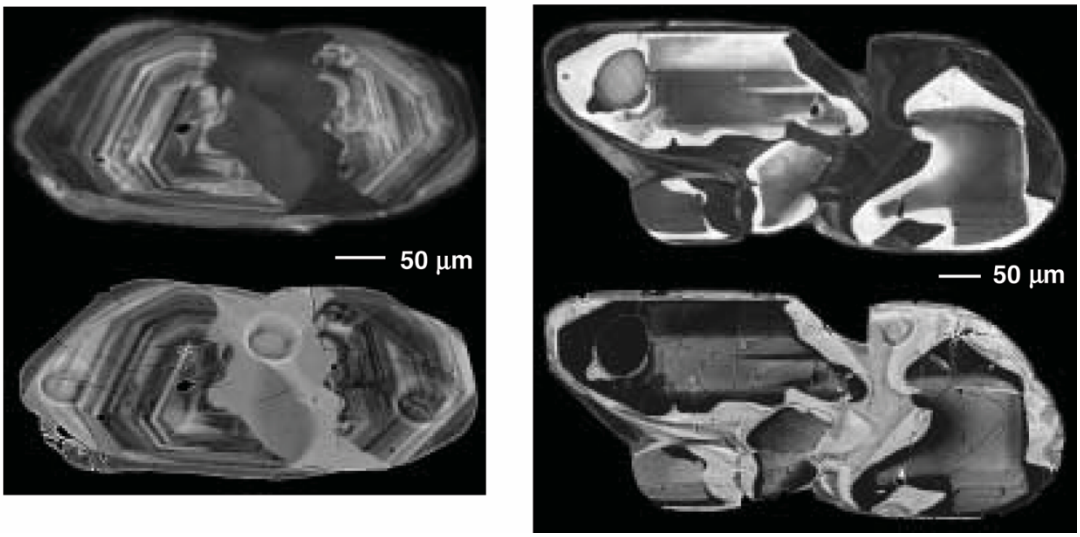

Figure 2

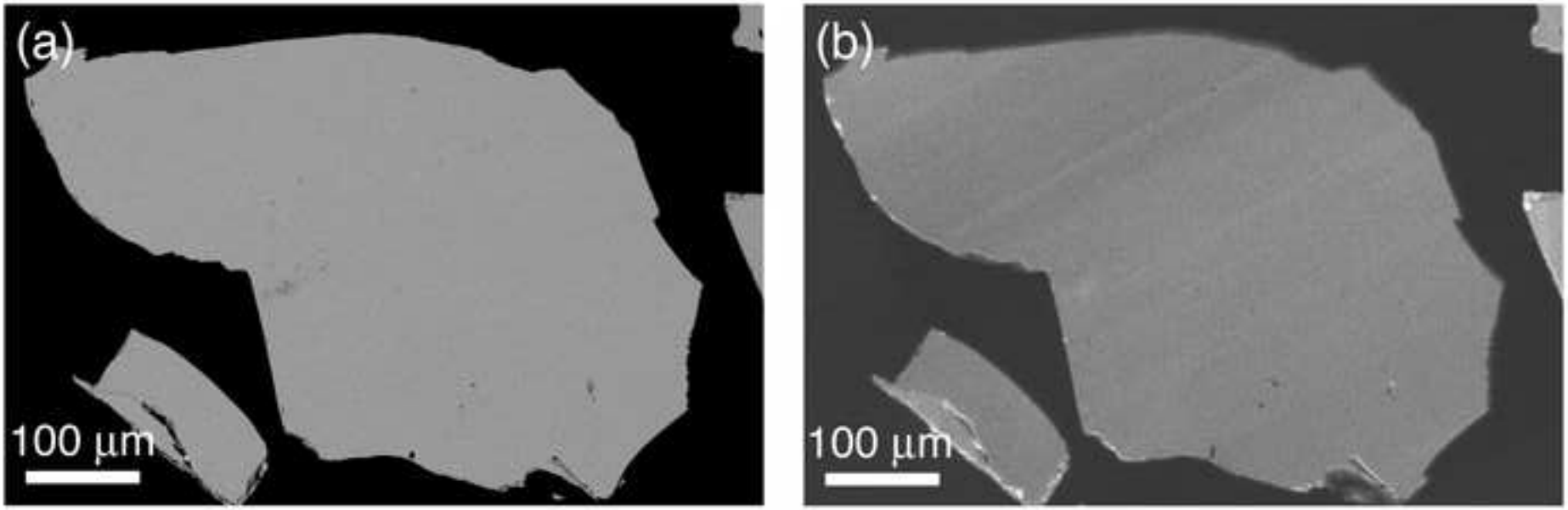

Figure 3

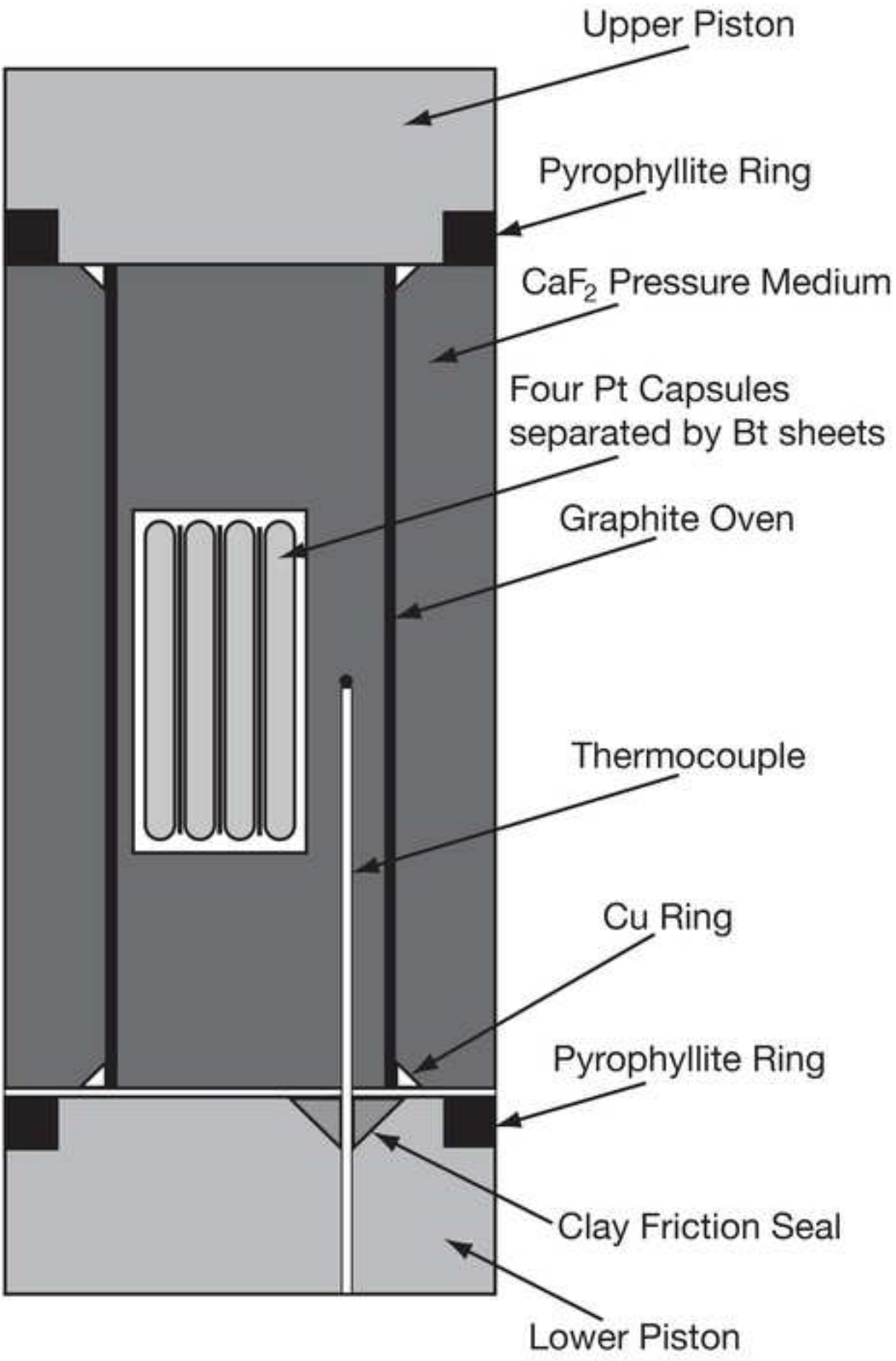

Figure 4

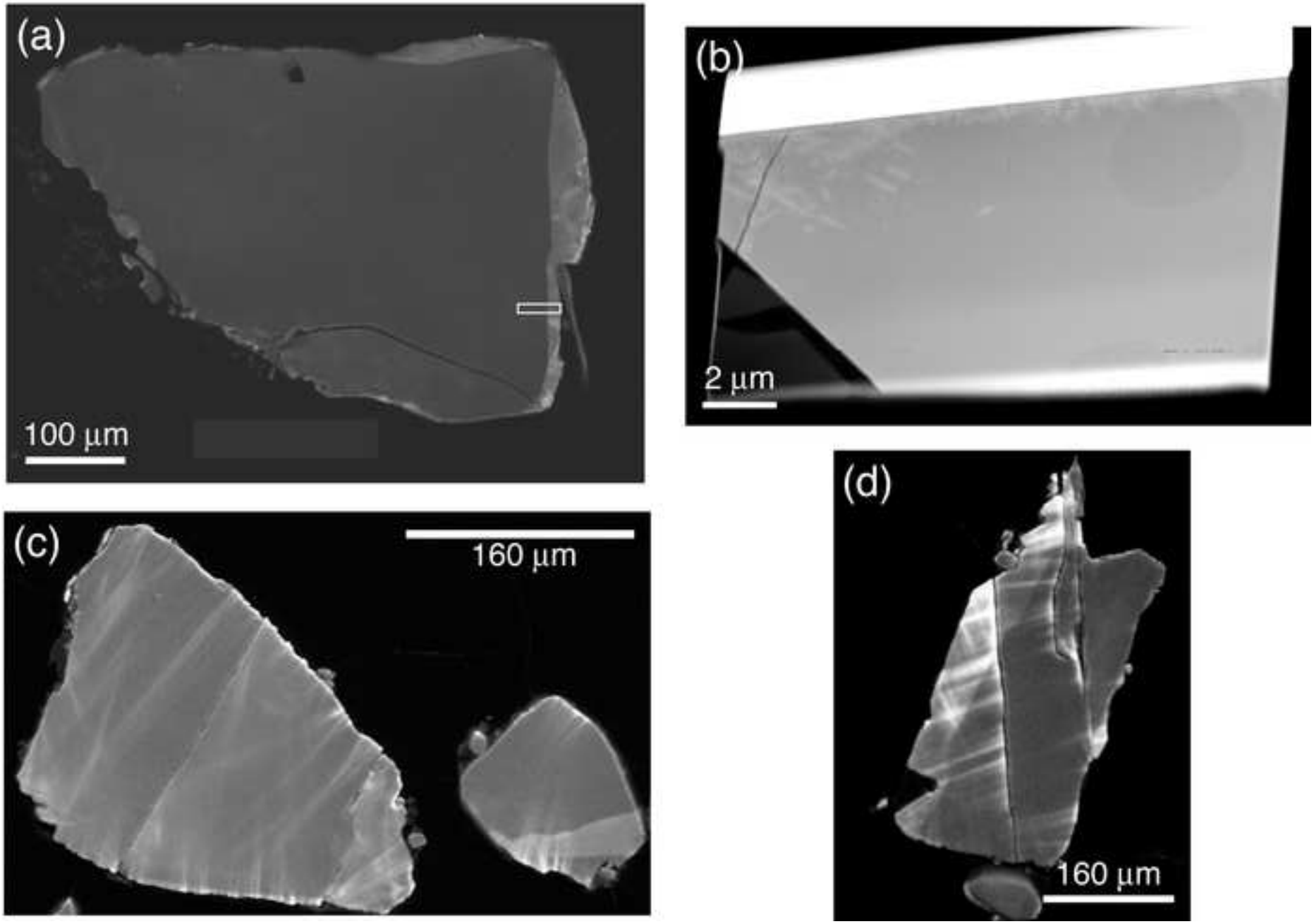

Figure 5

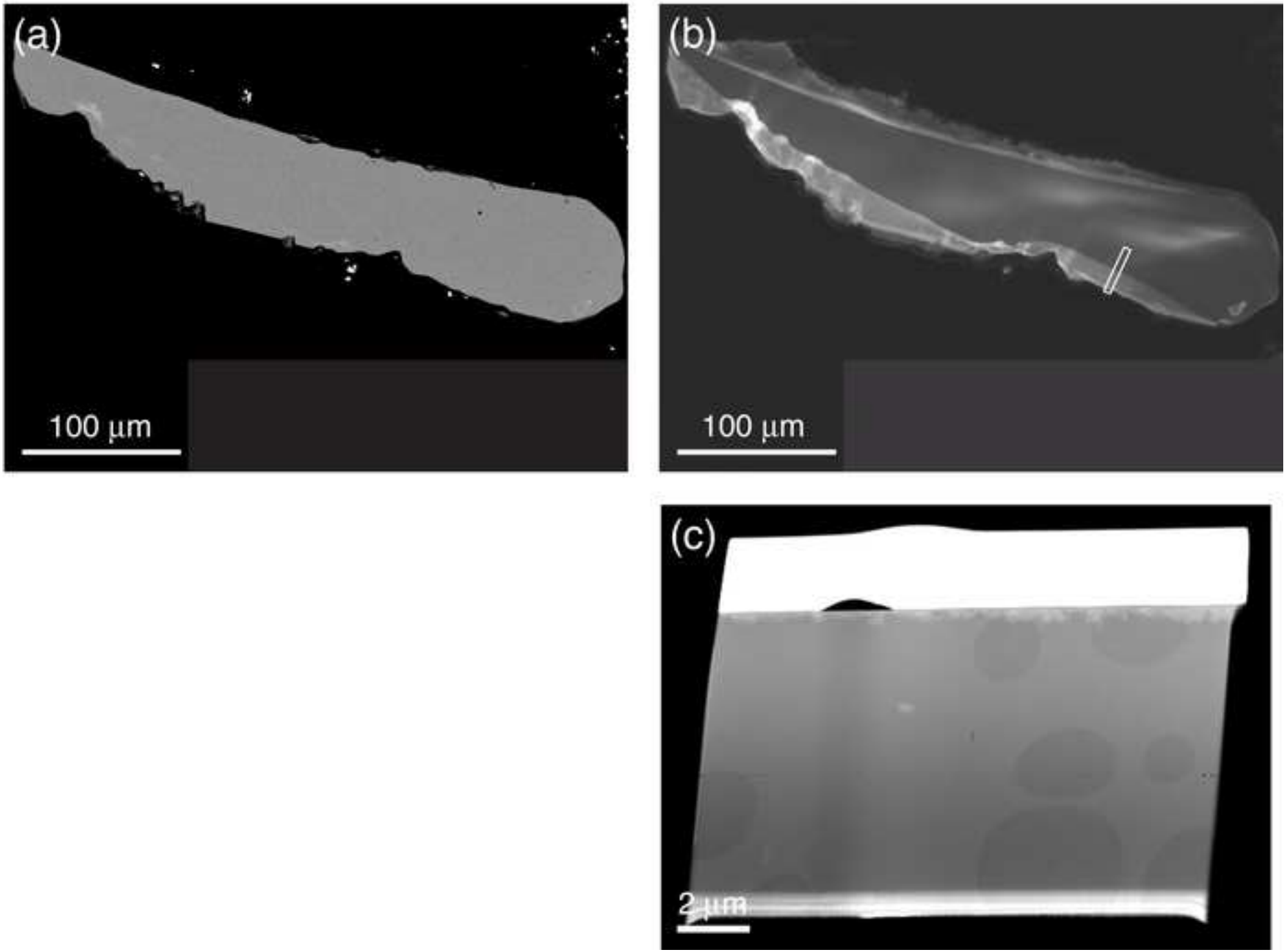

Figure 6

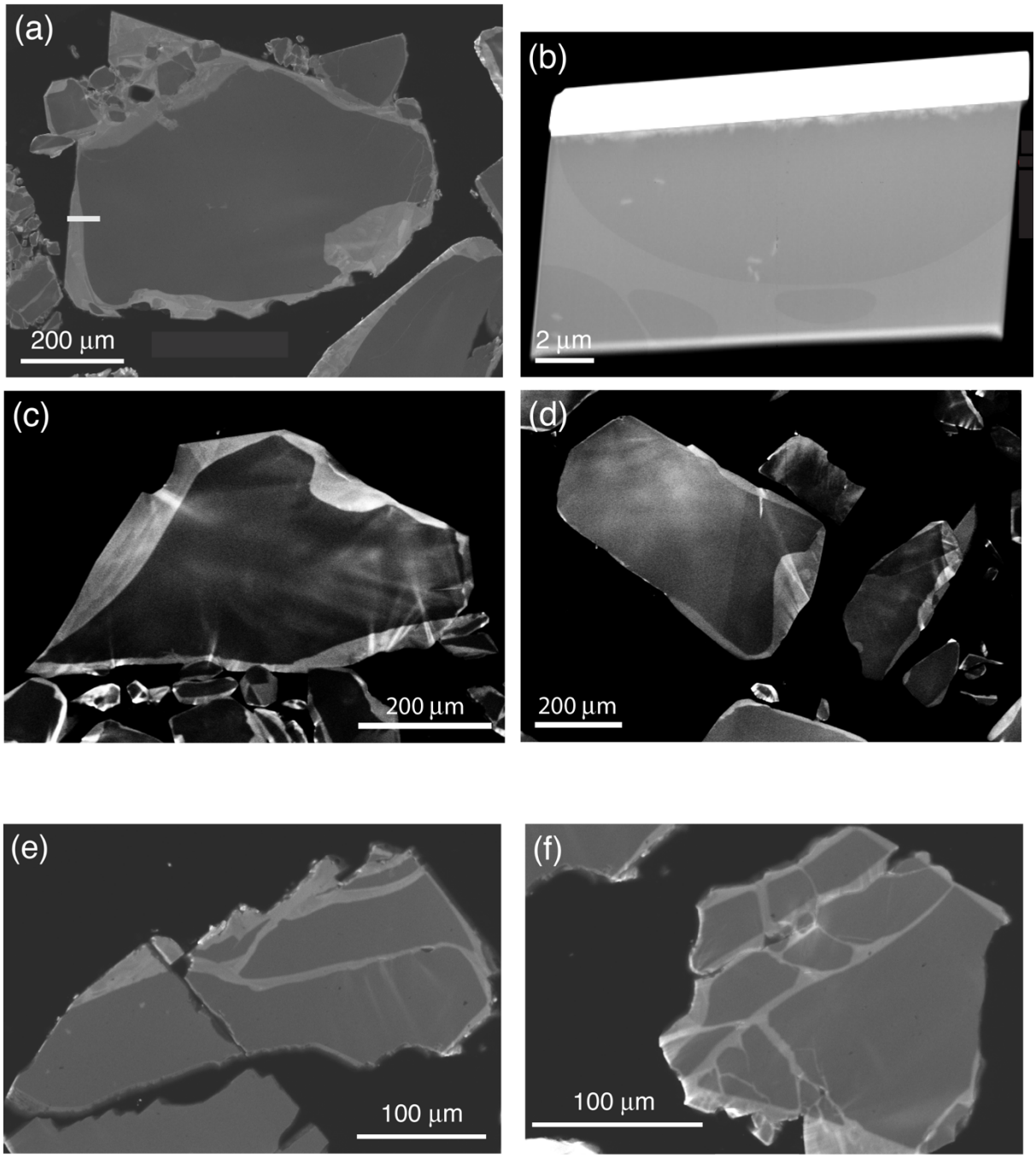

Figure 7

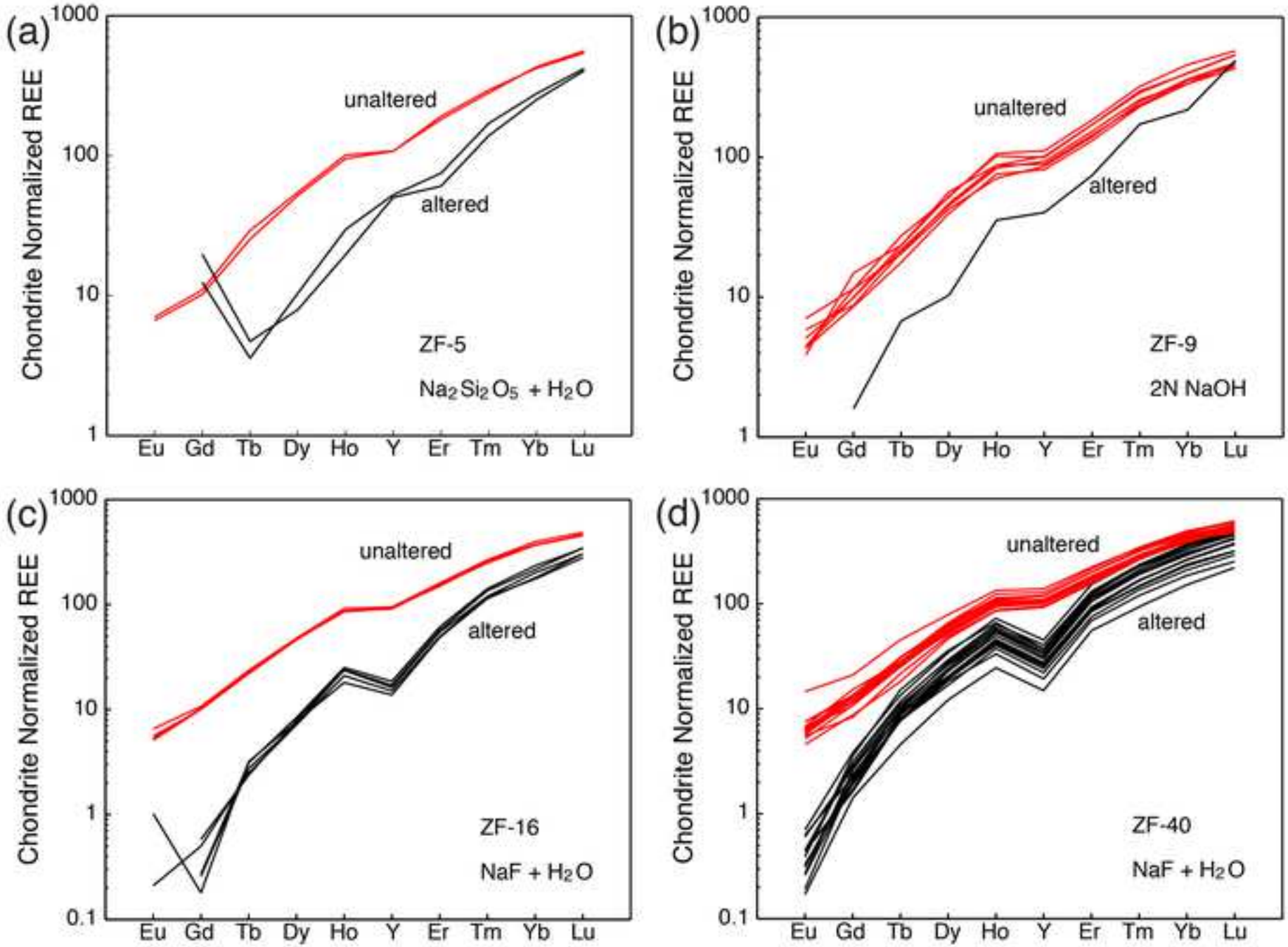

Declaration of interests

☒ The authors declare that they have no known competing financial interests or personal relationships that could have appeared to influence the work reported in this paper.

☐The authors declare the following financial interests/personal relationships which may be considered as potential competing interests: